

Modelling intergalactic low ionisation metal absorption line systems near the epoch of reionization

Teresita Suarez ¹  & Avery Meiksin ¹

¹*SUPA†, The Royal Observatory, Edinburgh, Blackford Hill, Edinburgh EH9 3HJ, UK*

Accepted XXX. Received YYY; in original form ZZZ

ABSTRACT

We interpret observations of intergalactic low ionisation metal absorption systems at redshifts $z \gtrsim 5$ in terms of pressure-confined clouds. We find clouds confined by the expected pressure of galactic haloes with masses $11 < \log M_h/h^{-1}M_\odot < 12$ provide a good description of the column density ratios between low ionisation metal absorbers. Some of the ratios, however, require extending conventional radiative transfer models of irradiated slabs to spherical (or cylindrical) clouds to allow for lines of sight passing outside the cores of the clouds. Moderate depletion of silicon onto dust grains is also indicated in some systems. The chemical abundances inferred span the range between solar and massive-star dominated stellar populations as may arise in starburst galaxies. The typical H I column densities matching the data correspond to Damped Lyman- α Absorbers (DLAs) or sub-DLAs, with sizes of 40 pc to 3 kpc, gas masses $3.5 < \log M_c/M_\odot < 8$ and metallicities $0.001 - 0.01Z_\odot$. Such systems continue to pose a challenge for galaxy-scale numerical simulations to reproduce.

Key words: absorption lines – reionization – intergalactic medium

1 INTRODUCTION

Cosmic reionization remains one of the paramount unsolved problems of modern cosmology. Observations of high redshift Quasi-Stellar Objects (QSOs) show the intergalactic medium (IGM) was reionized by $z = 5$ (Becker et al. 2015; Bosman et al. 2018). At higher redshift, evidence from QSO (Davies et al. 2018; Greig et al. 2017) and Lyman Break Galaxy (Mason et al. 2018) spectra suggest the IGM was largely neutral at $z \gtrsim 7.5$. Measurements of the Cosmic Microwave Background (CMB) require the IGM to have been ionised no earlier than $z \approx 8.4$, and suggest a midpoint reionization epoch of $z_{\text{re}} = 7.7 \pm 0.7$ (Planck Collaboration 2018).

The sources responsible for reionizing the IGM are unknown. Widely held to be star-forming galaxies, current evidence shows that the ionising emissivity of observed sources at $z > 5$ still falls short of what is required (Bouwens et al. 2015; Finkelstein et al. 2019). Whilst extending the luminosity function of observed galaxies to fainter systems produces the emissivity required to reionize the Universe, it is not clear that a sufficient fraction of photons manage to escape the galaxies (Puchwein et al. 2019). Some studies suggest that galaxies hosting active galactic nuclei contribute significantly to the ultraviolet background near the end of the reionization epoch at $z < 7$ (Giallongo et al. 2015; Finkelstein

et al. 2019), assuming essentially full escape of the ionising radiation produced.

Although the full complement of galaxies responsible for reionizing may be too dim to detect, they may be indirectly discovered through their impact on the IGM and their nature inferred. Models suggest material lost from the galaxies in winds enrich the IGM in metals (for reviews, see McQuinn 2016; Tumlinson et al. 2017). The chemical abundances of the inter-stellar and circum-galactic medium of the galaxies are expected to reflect the abundances of the stellar populations of the galaxies. The metal abundances of this enriched gas thus provide valuable insight into the nature of the earliest galaxies.

Numerical simulations suggest the first generation of stars after the Big Bang were very massive and were composed of pristine hydrogen and helium gas (Population III stars). Subsequent generations of stars formed from chemically enriched material but they are presumed to be metal-poor type stars (Population II stars), and their chemical abundance patterns will depend on their environments (eg Starkenburg et al. 2016). Modelling the stellar populations is further complicated by anomalies in the abundance patterns of metal-poor stars (Christlieb et al. 2002; Frebel et al. 2005; Norris et al. 2007), which show large overabundances in carbon and nitrogen of unclear origin. One suggestion is that gaseous regions with such overabundances are preferentially selected for forming stars as they provide the most

* Contact e-mail: tsuarez@ed.ac.uk

† Scottish Universities Physics Alliance

efficient conditions for gas to cool and fragment and form stars (Frebel et al. 2007).

Intergalactic metal absorption systems in the spectra of background quasars potentially provide a powerful probe of the composition of early stars and their environments. Measurements of element abundance ratios have been used to infer the nature of stellar populations in young galaxies (eg Becker et al. 2012).

At high redshifts the forest is too highly absorbed, becoming almost completely opaque by $z \sim 6$. The saturation of the absorption lines makes it impossible to make direct estimates of the metallicities for these systems. Instead, ionisation models of the absorption systems are necessary.

Early galaxies are expected to be surrounded by a reservoir of gas, from which they accrete and form stars. High HI column density intervening absorbers, especially sub-Damped Lyman Alpha (sub-DLAs, having $10^{19} < N(\text{HI}) < 10^{20.3} \text{ cm}^{-2}$) and Damped Lyman Alpha (DLAs, $N(\text{HI}) > 10^{20.3} \text{ cm}^{-2}$), may serve as probes of this gas. DLAs are found to have metallicities typically below $0.1 Z_{\odot}$ at intermediate redshifts $z \sim 2 - 4$ (Pettini et al. 1997; Prochaska et al. 2003) and rising above 0.1 solar metallicities at low redshift $z < 1.5$ (Rao et al. 2005). These previous studies indicate that the metallicities of DLAs decrease with increasing redshift (Wolfe et al. 2005). However, observations show a ‘floor’ in the metallicity of about $0.002 Z_{\odot}$ out to $z \sim 5$ (Wolfe et al. 2005; Rafelski et al. 2012), with rare exceptions (Ellison et al. 2010). Many metal-poor DLAs at intermediate redshifts $z < 4$ exhibit α -enhanced metallicities (Cooke et al. 2015; Rafelski et al. 2012).

Some systematic differences are found. Unlike their lower redshift counterparts, sub-DLA and DLA systems at $z > 5$ lack strong absorption by high ionisation species like CIV and SiIV, consistent with an evolving metallicity (Becker et al. 2011). On the other hand, low ionisation species like CII, SiII, FeII and OI show little evolution in their column density ratios over $2 < z < 6$ in some samples, with values similar to low metallicity non-carbon enhanced Pop II stars (Becker et al. 2012). Other samples, however, do show evidence for mild metallicity evolution for undepleted elements, with some systems at $z \sim 5$ having anomalously low [C/O] abundances (Poudel et al. 2018).

The low metallicities may be explained in a scenario in which star-forming galaxies enrich their environments over time. Galaxies build up their stellar content by recycling mass from gas expelled by evolved stellar populations (which are metal-rich), but also from gas accreted from the IGM. The accretion is believed regulated by feedback processes that may expel material from galaxies, limiting star formation. Intervening metal absorption systems may thus shed insight on the processes that enrich the stellar populations of galaxies as well as pollute the environments of galaxies, such as by supernovae-driven galactic winds (see Somerville & Davé 2015, for a review).

Feedback may regulate not only the metallicity of the gas and stars, but their abundances as well. Abundances dominated by core-collapse supernovae will be α -enhanced compared with solar abundances, an effect that may be enhanced in more massive galaxies as a result of feedback by Active Galactic Nuclei (AGN) (Segers et al. 2016).

Cool clouds in the Circumgalactic medium (CGM) may be highly transient, requiring constant replenishment of new

material from their host galaxies. Models for the origin of the clouds include formation in gaseous outflows, inflows and *in-situ* formation (eg Oppenheimer et al. 2012; Suresh et al. 2015; Suarez et al. 2016; Turner et al. 2017). The physics of the cool CGM is unresolved in cosmological hydrodynamic simulations. The physical scale of the clouds is estimated from observations to be as small as tens of parsecs, and possibly smaller, at low redshifts $z < 3$ (Prochaska & Hennawi 2009; Lan & Fukugita 2017). Such short scales pose a challenge for galaxy-scale hydrodynamical simulations (Peeples et al. 2019; Sparre et al. 2019). Recourse must instead be made to semi-analytic modelling. Estimated cloud masses for spherical models of circumgalactic sub-DLA and DLA systems pressure-confined in galactic haloes range from 100 to $10^8 M_{\odot}$, increasing with HI column density, and with sizes from 10 to several hundred parsecs (Lan & Mo 2019).

In this paper, we investigate the metal abundances of high redshift ($z > 5$) low ionisation absorption systems in the context of pressure-confined clouds with the view of learning the nature of the stellar populations arising during cosmic dawn, as reflected by the surrounding gas they enriched. All of the systems we model are likely sub-DLA or DLAs, although confirming direct HI absorption measurements are not possible for many. Another advantage of examining systems at $z > 5$ is their reduced metallicities (Morrison et al. 2016), mitigating the complication of dust depletion and permitting a cleaner test of the pressure-confined cloud model.

We use the radiation transfer code CLOUDY (Ferland et al. 1998, 2017) to model the column density ratios. Rather than following the general practice of using the results from slab models as is, in this paper we instead roll the clouds into cylinders to approximate the changing relative ionisation fractions between elements expected in spherical systems. This extends the dynamic range of predicted column density ratios by considering lines of sight passing through a range of projected separations from the cloud centres, and may explain some of the scatter in the measured ratios. We also consider both solar chemical abundance ratios and abundances more typical of Pop II dominated starburst galaxies (Hamann & Ferland 1993).

This paper is organised as follows. In the next section, we describe the configuration of the models and the parameterisation we use. We then discuss the characteristics and motivation of modelling absorption systems as pressure-confined clouds in Sec. 3. We compare our models to current available observations of metal absorption systems at $z \gtrsim 5$ in Sec. 4. We discuss our results in Sec. 5 and present our conclusions in Sec. 6.

2 CONFIGURATION OF THE MODELS

We model clouds in the circumgalactic medium of galaxies using the spectral synthesis code CLOUDY v.17.01 (Ferland et al. 1998, 2017).

We work under the assumption that non-isobaric clouds would restore pressure balance by fragmenting into smaller clumps of gas (Lan & Mo 2019). The models described here adopt the pressure at the illuminated face of the cloud and force the pressure to be kept constant throughout the cloud. We refer to the systems described here as pressure-confined models.

$\log n_{\text{H}}$ cm^3	$\log N(\text{HI})$ cm^{-2}	Radiation background	Redshift z	Metallicity Z	Geometry
[-3.0,-1]	20	H&M 2012	5	solar	slab
	21	H&M 2005	6	starburst	circular

Table 1. CLOUDY input parameters to model the physical properties of isobaric clouds in the CGM; n_{H} , $N(\text{HI})$ and H&M are the gas hydrogen density, the neutral hydrogen density and the radiation continuum by Haardt & Madau (2012, 2005), respectively. (Each column represents options independent of the option chosen in any other column.)

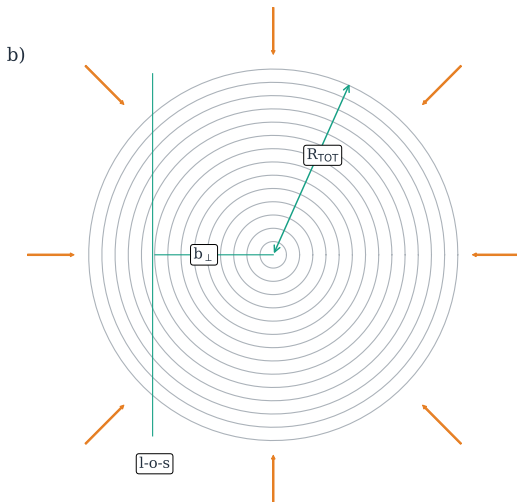
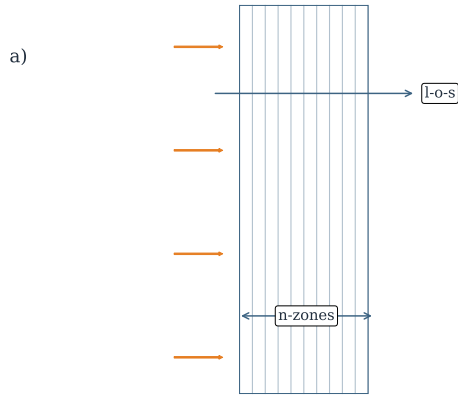


Figure 1. a) Slab geometry. This model assumes an infinitely broad flat cloud with an external radiation field impinging perpendicularly on one side. b) Circular cloud: radiation hits the cloud from all directions perpendicular to its surface.

Modelling metal absorption systems using CLOUDY allows specification of the radiation field shape and intensity. In our models we assume a UV background with contributions from quasars (QSOs) and galaxies using a background continuum from a Haardt & Madau table (Haardt & Madau 2012) at different redshifts. We initially explored a wide range of cloud densities values, n_{H} , then narrowed

solar (\odot)		starburst (Sb)	
Element	log	Element	log
H	0.0000	H	0.0000
C	-6.611	C	-7.104
Si	-7.460	Si	-7.465
O	-6.310	O	-6.182
Fe	-7.550	Fe	-8.234
Al	-8.530	Al	...
Mg	-7.460	Mg	-7.466

Table 2. Abundances specified by CLOUDY for the composition of default solar composition abundances and for a stellar population dominated by massive stars (using the *starburst abundances* option in CLOUDY). The *starburst abundances* values are for an evolving starburst galaxy from Hamann & Ferland (1993). The metallicity of the gas is relative to a solar Si abundance, with metallicity set at $Z = 0.001Z_{\odot}$.

the range by requiring physical stability and to match measured metal column density ratios and limits. As we shall see, the cloud densities are consequently restricted to the range $-3 < \log n_{\text{H}} < -1$. This is the density at the surface of the cloud, as it will usually increase interior to the cloud to maintain constant pressure.

These models stop the calculation when reaching a column density of neutral hydrogen equivalent to $10^{20} - 10^{21} \text{ cm}^{-2}$ from surface to centre, to approximate sub-DLA and DLA systems. We reference the model with the HI column densities set to one of these values in tables and figure legends. In agreement with previous modelling, we find that the low ionisation metal column density ratios require high neutral hydrogen column densities typical of DLAs (eg Becker et al. 2011). We also explore the effect of metal abundances by examining both models with solar abundances and with chemical abundances typical of an evolving starburst in a massive elliptical galaxy with a top-heavy stellar initial mass function, based on the galactic chemical evolution model M5a of Hamann & Ferland (1993), implemented using the ‘Abundances starburst’ option in CLOUDY.

The geometric configuration used by CLOUDY is a spherical gaseous shell surrounding a central source. A plane parallel slab with a radiation field impinging perpendicularly to the surface is approximated by asserting an extremely large radius for the shell compared with its thickness (the slab geometry). The inverse problem of a spherical cloud embedded in an external radiation field, the case of interest to the study of optically thick intergalactic absorption systems, is not available. Models of intergalactic absorption systems are usually computed using the slab geometry set-

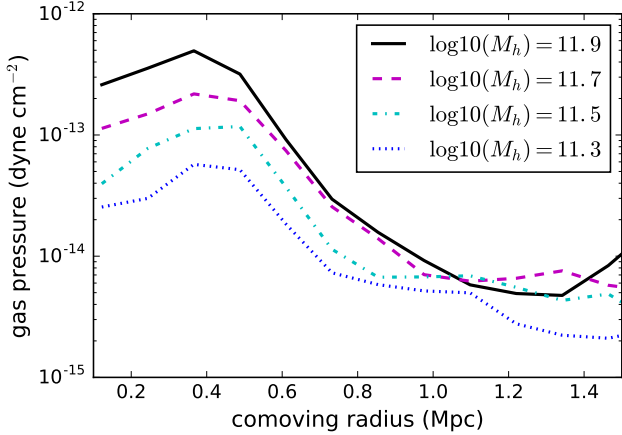


Figure 2. Gas pressure around dark matter haloes of masses between 10^{11} and $10^{12} h^{-1} M_{\odot}$ at $z \approx 6$, from the Sherwood simulation suite (Bolton et al. 2017).

ting, and column densities are computed along a normal to the slab surface. This fails to capture the actual ionisation layering within a spherical cloud and the column density ratios that would arise along lines of sight with impact parameters displaced from the cloud centre. To approximate such lines of sight, we “roll” the slab into a cylinder, allowing us to compute the column densities for ions along lines of sight displaced from the cloud centre, as shown in Fig. 1. As we shall show, variations in ion column density ratios arise as the impact parameter is changed. The variations will also depend on the confining pressure and size of the absorbers, so that measured column density ratios may be used to constrain these properties.

In Table 1 we summarise the values of the model parameters used. They are restricted by several physical considerations, as described in the following section.

3 PHYSICAL CHARACTERISTICS OF PRESSURE-CONFINED CLOUDS

In this section we analyse the physical characteristics of pressure-confined clouds. We describe the variations in ionisation fractions with radius based on CLOUDY models, and describe some of the considerations limiting the cloud properties.

Because galaxies are expected to reside in extended, overdense structures, the associated gas will be at much higher pressure than in the diffuse IGM. Although there are no direct measurements of the gas pressure in the haloes of high redshift star-forming galaxies, estimates may be made from cosmological simulations. Radially averaged gas pressure profiles at $z \approx 6$ from the Sherwood simulation suite (Bolton et al. 2017) are shown in Fig. 2 for a Λ CDM cosmology. Galactic wind feedback is included, following the prescription of Puchwein & Springel (2013), which is found to reproduce the rising HI absorption signature measured in the CGM of star-forming galaxies at $z \approx 3$ (Meiksin et al. 2017). Thermal gas pressures at distances $20 - 100$ kpc (proper) from the halo centres of $10^{-14} - 10^{-12}$ erg cm^{-3} are predicted for systems with halo masses between $10^{11} - 10^{12} h^{-1} M_{\odot}$,

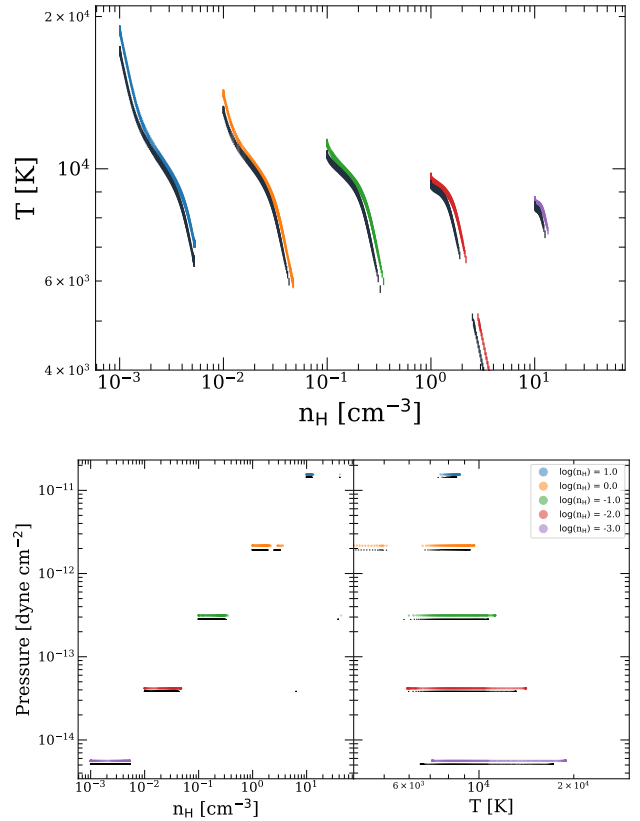


Figure 3. Physical properties of pressure-confined clouds. The top panel shows the temperature as a function of hydrogen density internal to the clouds. The bottom panel shows the ranges in density and temperature for selected isobaric models. The coloured lines are for clouds photoionised by a metagalactic field at $z = 6$ (Haardt & Madau 2012). Black lines are models using the metagalactic field at $z = 7$.

the characteristic halo mass range believed associated with DLAs for at least moderate redshift systems (Font-Ribera et al. 2012; Barnes & Haehnelt 2014).

Following earlier models (Lan & Mo 2019; Mo & Miralda-Escude 1996), we assume the clouds are confined by the pressure of the haloes. By choosing the hydrogen density at the surface of the cloud, a pressure is computed at the illuminated cloud surface required for thermal equilibrium. The pressure is forced to remain constant at this value throughout the cloud interior.

Fig. 3 illustrates the behaviour of the density and temperature interior to the clouds for different assumed densities at the surface, along with the required pressure resulting from thermal equilibrium. The top panel of Fig. 3 shows the temperature as a function of internal hydrogen density, n_{H} for different clouds. The bottom panel of Fig. 3 shows the ranges in hydrogen density and temperature interior to each cloud model for models with different pressures. The coloured curves are for models photoionised by the metagalactic radiation field of Haardt & Madau (2012) at $z = 6$, and the black lines show how these curves would change with variations in the ultra-violet background (UVB), for which we take the extragalactic background from Haardt &

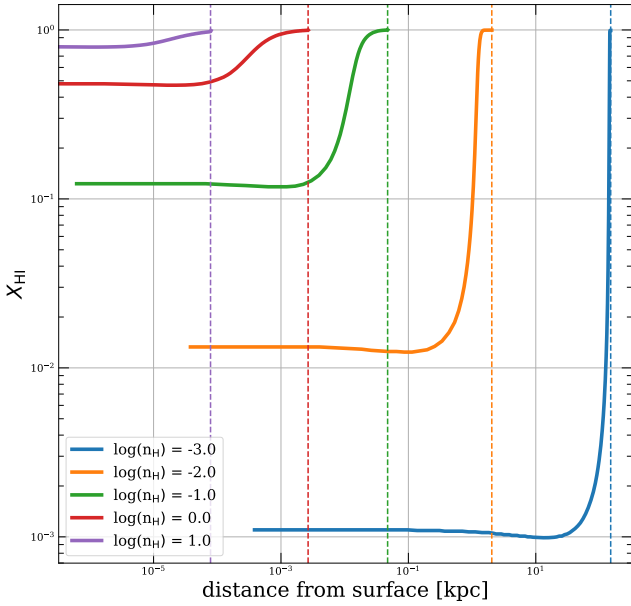


Figure 4. Fraction of neutral hydrogen (HI) as a function of distance from the cloud surface. The line colours correspond to different values in the surface hydrogen density. Lower hydrogen densities produce larger clouds. The hydrogen densities n_{H} are in cm^{-3} .

Madau (2012) at redshift $z = 7$ as an illustration. Only mild sensitivity to the external radiation field is found.

Fig. 4 depicts the variation in the neutral hydrogen fraction with distance from the cloud surface for different values of the surface hydrogen density n_{H} . The higher n_{H} is, the smaller the cloud radius. The difference in radii spans six orders of magnitude. A brief description of these models is: the cloud with surface density $n_{\text{H}} = 10 \text{ cm}^{-3}$ (purple curve) has a neutral hydrogen fraction of $X_{\text{HI}} = 0.8$ at the surface. The cloud radius is $< 1 \text{ pc}$. Next, a surface density $n_{\text{H}} = 1 \text{ cm}^{-3}$ gives a cloud with radius $R_{\text{c}} \sim 2.5 \text{ pc}$. It is about half ionised at its surface, quickly rising to being almost fully ionised at half its radius. Clouds with $n_{\text{H}} = 0.1 \text{ cm}^{-3}$ (green curve) reach a size of $\sim 50 \text{ pc}$. The surface neutral fraction is low, $X_{\text{HI}} \approx 0.1$, reaching 0.9 at the half radius. Models with $n_{\text{H}} = 0.01 \text{ cm}^{-3}$ (yellow curve) show a more bimodal behaviour. The cloud remains mostly neutral from its centre to its half radius. Outside the half radius, the neutral fraction climbs rapidly, reaching $X_{\text{HI}} = 1$ at three quarters of the cloud radius. Finally, the model with $n_{\text{H}} = 0.001 \text{ cm}^{-3}$ (blue curve) shows a size of $R_{\text{c}} = 150 \text{ kpc}$. The fraction of neutral hydrogen X_{HI} remains close to zero almost throughout the cloud, transitioning rapidly to $X_{\text{HI}} = 1$ only within 10 kpc of its centre.

Fig. 5 shows the variation in ionisation fraction with distance from the cloud surface for low-ionisation elements (OI, FeII, CII and SiII; top panel) and high-ionisation elements (CIV and SiIV; bottom panel). For comparison we also show the ionisation fraction of HI. The values shown in Fig. 5 are for a cloud with a column density of $\log N(\text{HI}) = 10^{20} \text{ cm}^{-2}$, starburst abundances and metallicity of 0.001 relative to solar. The Haardt & Madau (2012) radiation field at $z = 6$ is used.

The trends in the ionisation fractions depend on the

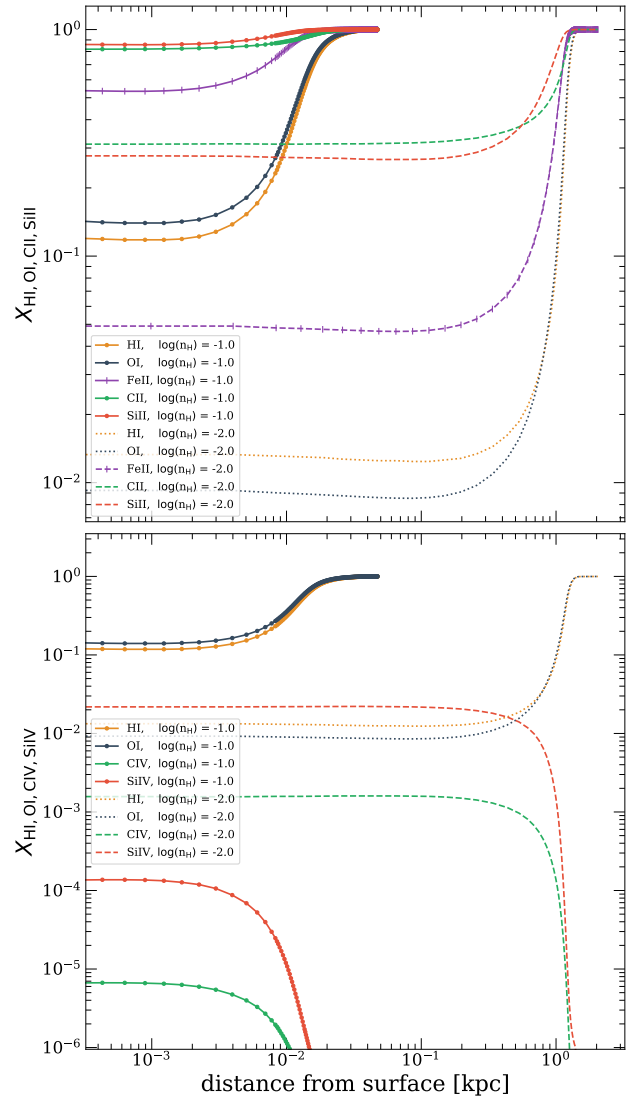


Figure 5. An example of the ionisation fractions of elements, X_{ion} , as a function of distance from the cloud surface. The top panel shows the ionisation fraction of HI and the low-ionisation elements FeII, CII, OI and SiII for two different hydrogen densities $n_{\text{H}} = 0.1, 0.01 \text{ cm}^{-3}$. The bottom panel shows the high-ionisation ions CIV and SiIV. We show the fractions of HI and OI for comparison. We set the densities also to $n_{\text{H}} = 0.1, 0.01 \text{ cm}^{-3}$. These fractions were generated by a model with $N(\text{HI}) = 10^{20} \text{ cm}^{-2}$, metallicity from massive stars and a radiation field at $z = 6$ using a H&M 2012 model.

cloud model. For the higher density case, $n_{\text{H}} = 0.1 \text{ cm}^{-3}$, the cloud radius is $R_{\text{c}} \sim 50 \text{ pc}$. The ionisation fractions of CII and SiII are high, remaining at $X_{\text{CII, SiII}} > 0.8$, through the entire cloud. The ratio of $N(\text{SiII})$ to $N(\text{CII})$ varies with depth, with $X_{\text{SiII}} \sim 1.0$ one-fifth the way into the cloud, while $X_{\text{CII}} \sim 1.0$ only within the inner half of the cloud. The fractions of HI and OI start to grow $\sim 10 \text{ pc}$ from the surface. Having nearly identical ionisation potentials, they closely track each other, reaching $X_{\text{HI, OI}} > 0.8$ at the half radius. The high-ionisation elements (CIV and SiIV), bottom panel of Fig. 5,

are negligible, both below 2×10^{-4} , and vanishingly small in the inner half of the cloud.

Somewhat different trends for low-ionisation ions are found for a surface hydrogen density $n_{\text{H}} = 0.01 \text{ cm}^{-3}$. This cloud is substantially larger, with a radius of about ~ 2 kpc. Although the CII fraction slightly exceeds the SiII fraction near the cloud surface, the SiII fraction increasingly dominates one-third the way into the cloud until they both reach unity at the cloud centre. The HI and OI fractions are at the percent level from the surface to half radius, both increasing rapidly thereafter. Compared with the previous denser cloud, the ionisation fractions of the high-ionisation elements CIV and SiIV are much higher, but plummet to vanishingly low levels within the inner half of the cloud (bottom panel of Fig. 5).

We also test the stability of the cloud by calculating the Jeans length (λ_{J}) for each model,

$$\lambda_{\text{J}} \simeq c_{\text{s}} (4\pi G m_{\text{p}} n_{\text{H}})^{-1/2} \quad (1)$$

where c_{s} is the speed of sound, G is the gravitational constant and m_{p} is the mass of a proton (Spitzer 1978). The values for the radii and masses of the clouds and Jeans length for relevant models are summarised in the model tables below. Only Jeans stable systems are used. (Note that ‘log’ values are in base 10.) A lower limit on cloud mass imposed by thermal heat conduction is estimated at around $10^3 - 10^4 M_{\odot}$, below which pressure-confined clouds evaporate on the timescale of tens to several hundred million years (Armillotta et al. 2017; Lan & Mo 2019).

4 COMPARISON WITH OBSERVATIONS

We use measurements of the low ionisation species of carbon, oxygen, silicon and iron in intervening absorption systems at $z \gtrsim 5$ from Becker et al. (2011, 2012); D’Odorico et al. (2013); Ryan-Weber et al. (2009); Morrison et al. (2016); Poudel et al. (2018, 2019); Bañados et al. (2019) to constrain the physical properties of the absorbers. We provide a compilation of the data used in Appendix A: Tables A1, A3, A4 and A5.

We first compare with the data of Becker et al. (2012). The metal line measurements were taken using the Keck/HIRES (FWHM = 6.7 km s^{-1}), Keck/NIRSPEC (FWHM $\sim 15 \text{ km s}^{-1}$), Magellan/MIKE (FWHM = 13.6 km s^{-1}) and VLT/X-Shooter ($\sim 30 \text{ km s}^{-1}$) spectrometers. We also compare with two very low metallicity ($Z \sim 0.001 Z_{\odot}$) proximate DLA systems at $z \gtrsim 6$. One measured in the spectrum of the QSO J2310 using the X-Shooter spectrometer with a resolution of 8800 has redshift $z \simeq 5.939$, blueshifted relative to the systemic QSO redshift by $\sim 2750 \text{ km s}^{-1}$ with $\log N(\text{HI}) = 21.05 \pm 0.1$ (D’Odorico et al. 2018). The second system was detected in the spectrum of QSO P183+05 that was selected in the Pan-STARRS1 survey (Chambers et al. 2016) at $z = 6.4$ (Bañados et al. 2019). The absorber is blueshifted relative to the QSO systemic redshift by only 1400 km s^{-1} , or at a distance of 1.8 Mpc in front of the QSO if the velocity is interpreted as Hubble expansion. The HI column density measured in the QSO spectrum exceeds $10^{20.5} \text{ cm}^{-2}$, but it is unclear how much of this arises in the absorption system and how much from the ambient IGM,

especially as the IGM may not be fully ionised at this redshift. The data are also consistent with the system being a sub-DLA in a mostly neutral IGM.

Motivated by previous findings that the column density ratios among CII, SiII, OI and FeII are consistent with (metal poor) sub-DLAs and DLAs (Becker et al. 2011, 2012), all our models use neutral hydrogen column densities of $N(\text{HI}) \sim 10^{20} - 10^{21} \text{ cm}^{-2}$, to represent the systems. We also explored the effect of using lower column densities, $\log N(\text{HI}) \lesssim 19$, but we find that the higher column densities improve the agreement with the observed ratios. Results for both solar and starburst chemical abundances for models matching the data are provided in Table 3.

Fig. 6 shows the column density ratios of the ions CII to OI and SiII to OI, for absorption systems at $4.7 < z < 6.3$. The colour bar indicates the impact parameter for the assumed line of sight, expressed as a fraction of the cloud radius (R_{c}): $b_{\text{frac}} = b_{\perp}/R_{\text{c}}$ (see Fig. 1). Purple corresponds to a line of sight close to the centre of the cloud and yellow is near the surface of the cloud. The value $b_{\text{frac}} = 0$ recovers the result for a line of sight perpendicular to the corresponding slab model (except the HI column density is doubled to account for the full cloud diameter). The models with solar abundance hit a floor in $\log [N(\text{CII})/N(\text{OI})]$ at about ~ -0.3 , corresponding to a line of sight passing through the centre of the DLA, where all the carbon is in the form of CII and the oxygen in the form OI. This is because radiation able to ionise neutral oxygen or singly ionised carbon is no longer able to penetrate to the centre of the cloud. Almost all the data of Becker et al. (2011) have smaller values. Whilst a broad range of larger ratios are possible for lines of sight at increasing impact parameters, these models move away from the measured values. Models are able to recover the measured ratios only by increasing the carbon to oxygen ratio, confirming the conclusion of Becker et al. (2011) that the composition of the clouds must be α -enhanced. Fig. 6, however, shows it is not necessary to move all the way to the chemical composition of a starburst: the clouds display intermediate compositions.

The proximate DLA reported by D’Odorico et al. (2018) shows several metal absorption lines, however they remark the lines are not resolved by X-Shooter and so may be saturated. The reported column densities for CII, SiII and OI none the less place the absorber near the trend for solar abundances, corresponding to values deep within a DLA core (orange point in Fig. 6).

The ratio of CII to OI for the proximate DLA from Bañados et al. (2019) is consistent with both solar and starburst abundances, but only for impact parameters passing through the outer half of a cloud if starburst abundances are assumed and a standard UVB intensity adopted. Such a possibility is consistent with the alternative sub-DLA interpretation of the measured absorption. The reported SiII to OI ratio places it squarely in the starburst abundance regime, distinct from the solar, as shown by the pink filled point in Fig. 6. Boosting the UVB by a factor of 4, as if there were local sources, would permit the line of sight to pass closer to the cloud core for $\log N(\text{HI}) = 20 \text{ cm}^{-2}$. There are, however, discrepancies between the three distinct SiII transitions detected, likely a result of contamination of some of the features. The authors suggest adopting the lower column density measured of $10^{13.5} \text{ cm}^{-2}$, and even accepting it

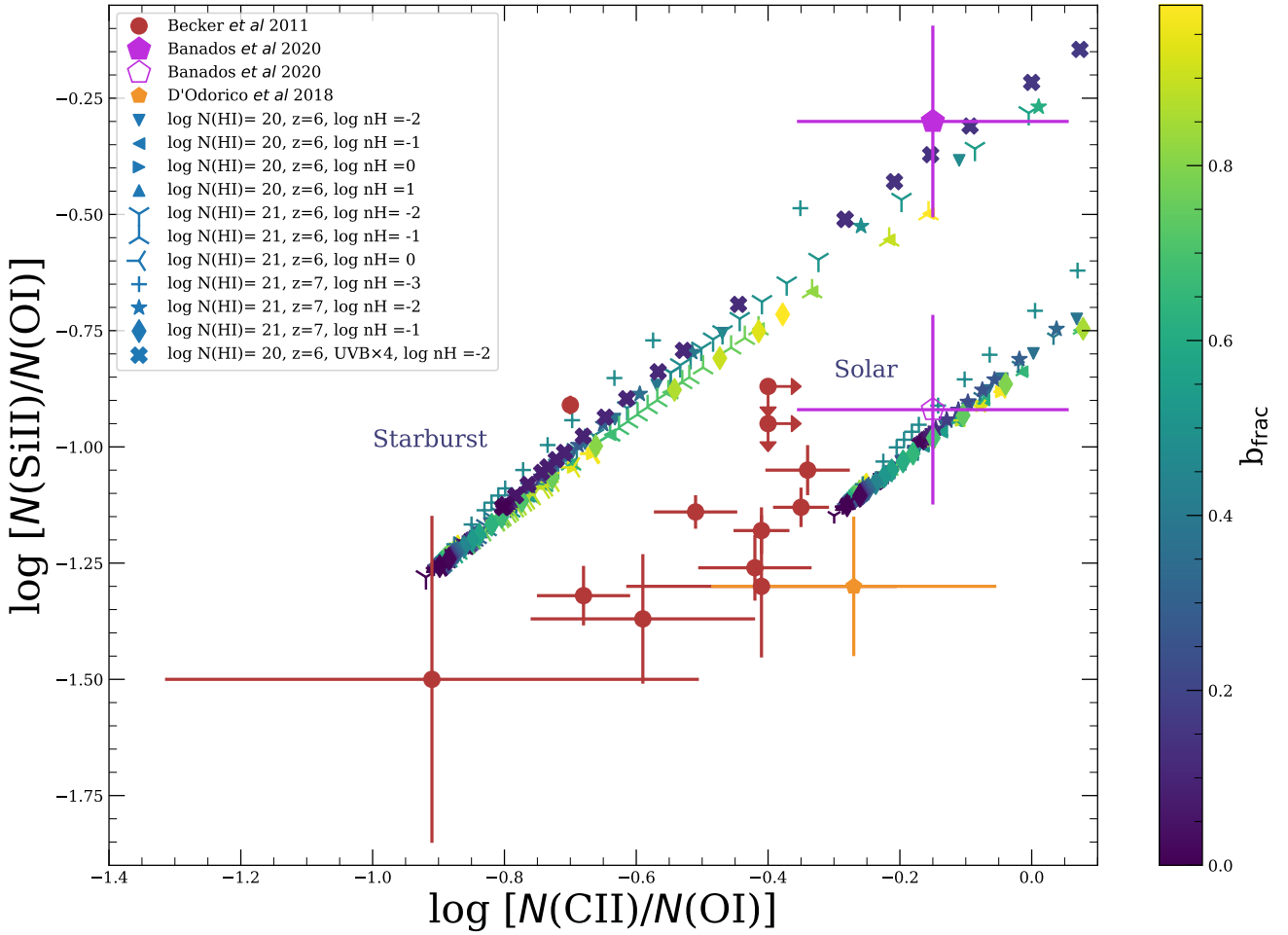


Figure 6. Column density ratios between SiII, CII and OI for data from Becker et al. (2012) (red circles), Bañados et al. (2019) (full and empty pink pentagons; the SiII values are upper limits, see text) and D’Odorico et al. (2018) (orange pentagon). Markers in colour are CLOUDY models corresponding to the legend, with a clear division between predictions for different abundances. Models have slab neutral hydrogen column densities $N(\text{HI})=20 \text{ cm}^{-2}$ and $N(\text{HI})=21 \text{ cm}^{-2}$. The surface hydrogen density (n_{H}) varies between 0.001 and 1 cm^{-3} . All models use a radiation background from Haardt & Madau (2012) at $z = 6$ and 7. The colour bar indicates the impact parameter of the line-of-sight measurement through the cloud, with dark blue corresponding to small impact parameters and light yellow to lines of sight passing near the cloud surface. The value $b_{\text{frac}} = 0$ recovers the slab models.

conservatively as an upper limit because of possible CIV contamination from another absorption system along the line of sight. We show this upper limit in Fig. 6 with the empty pink pentagon-type point. This decreases $\log[N(\text{SiII})/N(\text{OI})]$ to < -0.9 , in agreement with solar abundances, yet again preferentially for a line of sight passing outside a cloud core, where the HI and OI fractions have fallen, although the large error bars are consistent with a line of sight passing through a cloud core as well. The errors are marginally ($\sim 2\sigma$) consistent with starburst abundances.

Similar trends are found on comparing model predictions for the FeII to CII and SiII to CII ratios with the data, as shown in Fig. 7. The absorption systems from Becker et al. (2012) again lie between the predictions for absorption within DLA cores with abundances between solar and starburst, although some, with the lower values of $N(\text{FeII})/N(\text{CII})$, favour lines of sight with impact parameters offset from the cores. Allowing for an enhanced radiation field also introduces an ambiguity in interpretation, producing

matches to the data with higher values of $N(\text{FeII})/N(\text{CII})$ if along lines of sight displaced from the cloud cores for systems with solar abundances. This is opposite the trend for the SiII to OI and CII to OI ratios, suggesting intermediate abundances for the absorbers is the preferred interpretation.

Given the large FeII error bar for the proximate DLA of D’Odorico et al. (2018) (orange point), and the possibility the CII line is saturated, the system is again consistent with a line of sight through the core of a DLA with solar abundances. The FeII to CII and SiII to CII ratios for the proximate DLA of Bañados et al. (2019), accepting the larger SiII column density, is again consistent with a line of sight displaced from the core of an absorber with starburst abundances. Accepting the lower SiII as an upper limit, however, moves the point to $\log[N(\text{SiII})/N(\text{CII})] < -0.77$, in agreement with a sub-DLA interpretation with solar abundances, as above for the SiII to OI and CII to OI ratios.

Constraints from the upper limits placed on high-ionisation ions by Becker et al. (2011) are shown in Fig. 8.

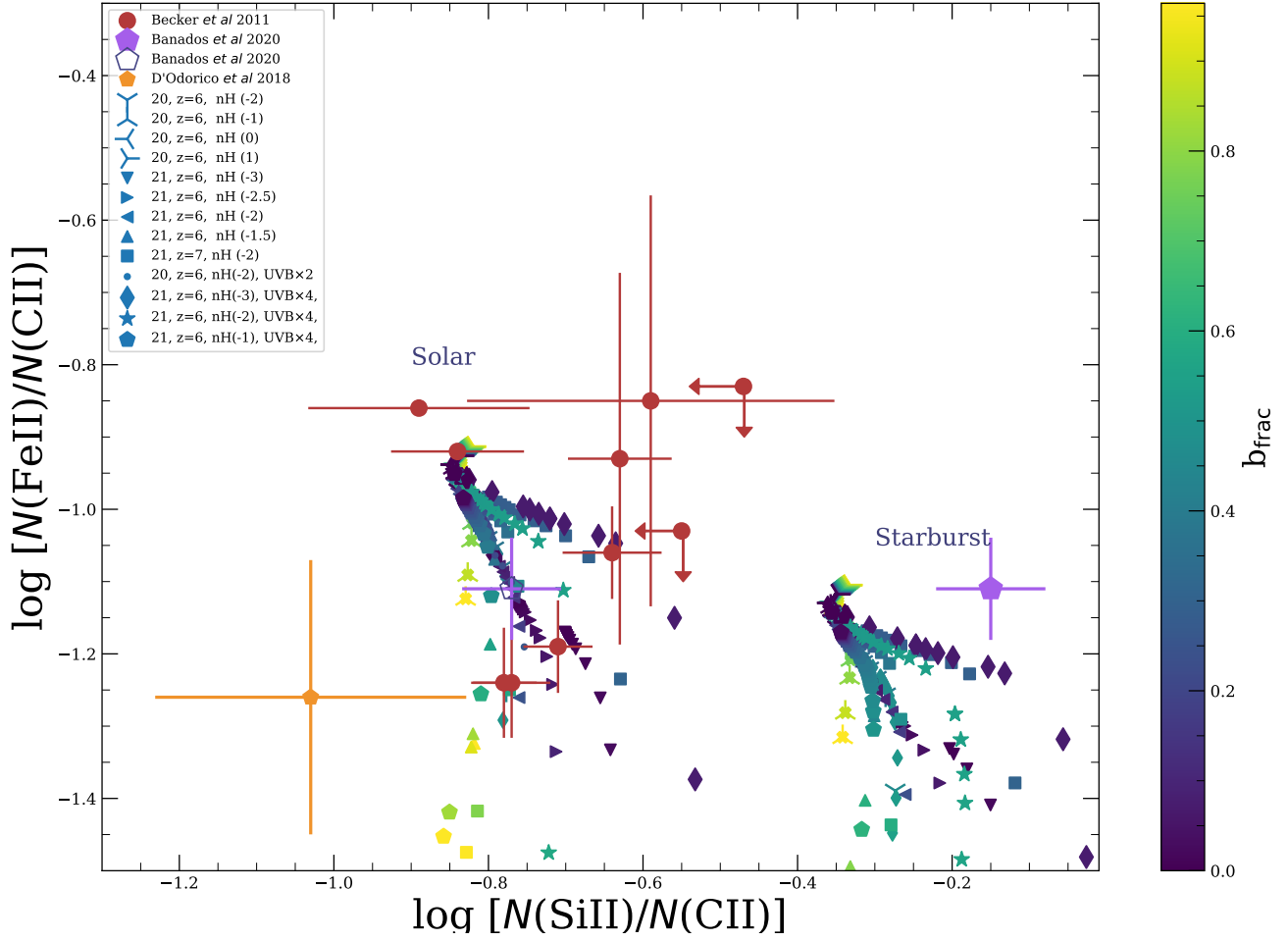


Figure 7. Column density ratios between FeII, SiII, CII for data from [Becker et al. \(2012\)](#) (red circles), [Bañados et al. \(2019\)](#) (full and empty pink pentagons); the SiII values are upper limits, see text) and [D'Odorico et al. \(2018\)](#) (orange pentagon). Markers in colour correspond to different CLOUDY models, indicated in the legend as in Fig. 6.

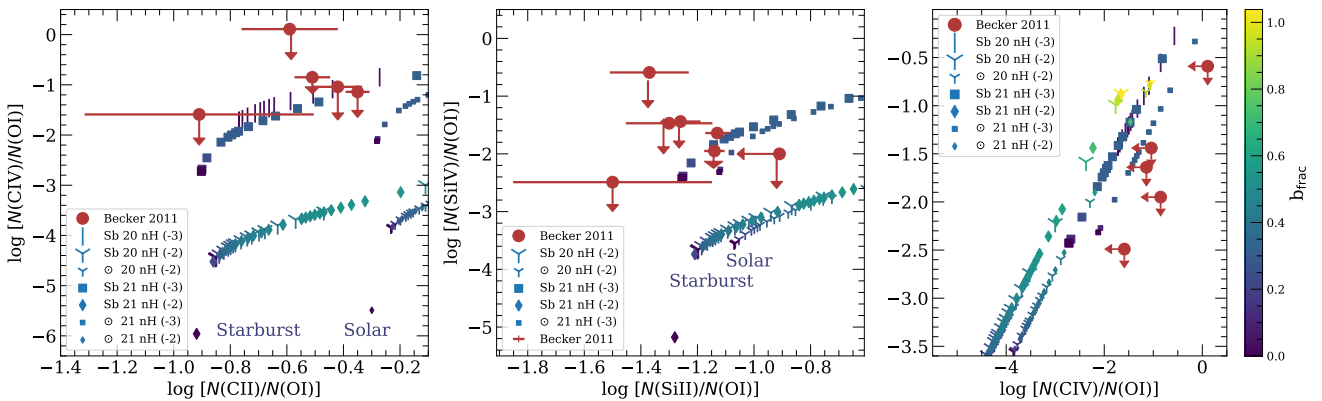


Figure 8. Data taken from [Becker et al. \(2011\)](#), all upper limits. Coloured markers indicate several combinations of parameters of the CLOUDY models. See properties in the legend box. There is a near degeneracy between solar and starburst abundances for some ratios. The colour bar indicates the impact parameter of the line-of-sight measurement through the cloud, with dark blue corresponding to small impact parameters and light yellow to lines of sight passing near the cloud surface. The value $b_{\text{frac}} = 0$ recovers the slab models. (left panel) Column densities of CIV to OI vs CII to OI. The values in the column densities for CIV systems are upper limits (red arrows). (middle panel) Column densities for SiIV to OI vs SiII to OI. Arrows indicate upper limits for SiIV; one data point indicates a lower limit in OI. (right panel) Column densities systems of SiIV vs CIV (both to OI).

Table 3. Top table: Column densities and their ratios (both expressed as log), for representative ionisation models using CLOUDY to model the data from Becker et al. (2012, 2011). (The metal column densities are normalised to $0.001Z_{\odot, Si}$ for both solar and starburst abundance models.) A subsample of the data in Figs. 6 and 7 is shown. Bottom table: The physical properties and parameters of the models: hydrogen density (n_{H}) in cm^{-3} , pressure (P) in dyne cm^{-2} , Jeans length (λ_{J}) in kpc, radius of the cloud (R_{c}) in kpc, mass of the cloud (M_{c}) in M_{\odot} , impact parameter (b_{\perp}), $b_{\text{frac}} = b_{\perp}/R_{\text{c}}$, radiation field redshift, abundance and input HI density for CLOUDY (log $N(\text{HI})$). The abundance column indicates starburst abundances (Sb) or solar abundances (\odot).

Model	HI	CII	OI	SiII	FeII	CIV	SiIV	CII/OI	SiII/OI	CIV/OI	SiIV/OI	FeII/CII	SiII/CII
1	20.30	13.34	14.11	13.04	12.12	12.39	12.69	-0.76	-1.06	-1.71	-1.42	-1.22	-0.29
2	20.30	13.27	14.12	12.92	12.10	9.67	10.45	-0.85	-1.19	-4.44	-3.66	-1.16	-0.34
3	17.82	11.56	11.71	11.22	10.24	6.46	7.42	-0.15	-0.49	-5.24	-4.29	-1.31	-0.34
4	20.27	13.82	13.96	13.03	12.78	12.86	12.67	-0.13	-0.92	-1.09	-1.28	-1.04	-0.79
5	17.52	12.30	11.05	11.38	10.54	9.99	10.28	1.24	0.33	-1.05	-0.76	-1.76	-0.91
6	20.30	13.76	13.99	12.92	12.78	10.14	10.43	-0.23	-1.06	-3.84	-3.55	-0.97	-0.83
7	20.07	13.49	13.76	12.64	12.55	6.76	7.16	-0.27	-1.12	-7.00	-6.60	-0.94	-0.84
8	21.29	14.20	15.11	13.85	13.07	11.89	12.18	-0.90	-1.26	-3.21	-2.92	-1.13	-0.35
9	20.15	13.11	13.98	12.77	11.96	8.91	9.61	-0.86	-1.20	-5.06	-4.36	-1.14	-0.34

Model	n_{H}	$\log P$	λ_{J}	R_{c}	$\log M_{\text{c}}$	b_{\perp}	b_{frac}	redshift	abundance	$\log N(\text{HI})$
1	0.001	-14.25	41.77	149.93	11.88	0.00	0.00	6	Sb	20
2	0.01	-13.37	11.42	2.03	7.61	0.03	0.01	6	Sb	20
3	0.1	-12.50	3.23	0.04	3.58	0.04	0.98	6	Sb	20
4	0.001	-14.24	41.84	146.07	11.85	2.13	0.01	6	\odot	20
5	0.01	-13.37	11.43	1.98	7.58	1.94	0.97	6	\odot	20
6	0.01	-13.37	11.43	1.98	7.58	0.03	0.01	6	\odot	20
7	0.1	-12.49	3.23	0.04	3.46	0.00	0.00	6	\odot	20
8	0.001	-14.29	39.88	128.38	12.13	4.30	0.03	7	Sb	21
9	0.01	-13.41	11.01	0.97	6.52	0.00	0.00	7	Sb	21

These provide consistency checks on the models inferred from the low-ionisation line ratios. The left and middle panels show the column density ratios of CIV and SiIV, each to OI, vs the column density ratios of the low-ionisation lines CII and SiII, each to OI. The high ionisation lines place an additional constraint on the density of the absorption systems, requiring $\log n_{\text{H}} > -3$. Combining the CIV and SiIV upper limits is consistent with this, as shown in the third panel.

Poudel et al. (2018) targetted three DLA systems at $4.8 < z < 5.4$, somewhat later in cosmic time than the systems above but still probing into the cosmic dawn era.

A summary of the observations is provided in Table A3, which shows the results from Voigt-profile fitting for three absorption systems at $z_{\text{abs}} = 5.335$ (SDSS QSO Q0231±0728), $z_{\text{abs}} = 4.809$ and 4.829 (Q0824+1302). All these systems show low-ionisation metal absorption features of CII and SiII and OI. We also include an earlier measurement of a sub-DLA at $z = 4.98$ in the spectrum of SDSS QSO Q1202+3235 using the Keck HIRES and ESI spectrometers (Morrison et al. 2016).

These samples were enhanced by another set of systems at $z > 4.5$, some now measured at very high spectral resolution (Poudel et al. 2019). The two quasars J1557+1018 and J1253+1046 were observed with MIKE at the Las Campanas observatory, QSO J1233+0622 was observed with VLT X-Shooter and QSO J0306+1853 was observed with MagE (Magellan Echelle). The spectral resolution for MIKE is $\sim 22,000$ -28,000, for X-Shooter is $R = 5300$ and for MagE is ~ 4100 ; (see Poudel et al. 2019, for details.).

The sample contains seven absorbers with neutral hy-

drogen column density of $\log N(\text{HI})=19.65$ to 20.75 , at redshifts from $z = 4.59$ to 5.05 along the sight lines to four quasars. Table A4 presents the results of Voigt-profile fitting for OI, CII, SiII and FeII. This is a subsample of all the reported measurements in Table 2 in Poudel et al. (2019), showing CII and SiII and at least one of OI or FeII.

In Fig. 9, we compare estimates for the column density ratios CII to OI and SiII to OI from different models, following the procedure described for Figs. 6 and 7, with the data from Morrison et al. (2016) and Poudel et al. (2018, 2019). We again consider both solar and starburst abundances. The top-left panel shows results for three absorption complexes observed at moderate spectral resolution that Voigt-profile fitting resolves into a few sub-components. The ratios drawn from the total column densities for the complexes are shown as red points. We next discuss these complexes and their components.

The absorber at $z_{\text{abs}} = 5.335$ is fit by two sub-components (yellow points; data taken from Table 2 in Poudel et al. 2018). One individual sub-component from this dataset is matched by models with solar abundances (such as Model 8 in Table 4). The other sub-component lies closer ($\sim 3\sigma$) to the models using starburst abundances, however it still has an offset of ~ 0.2 dex from the starburst models and no model provides a good fit: the SiII to OI ratio is too low. Using the total column densities for this system, however, the ratios agree with a solar abundance model with $\log n_{\text{H}} = 1 \text{ cm}^3$ (red point with the smallest error bars). We are not able to push the hydrogen density to higher values, as CLOUDY stops the calculation because the electron temperature reaches its lowest possible value for an isobaric

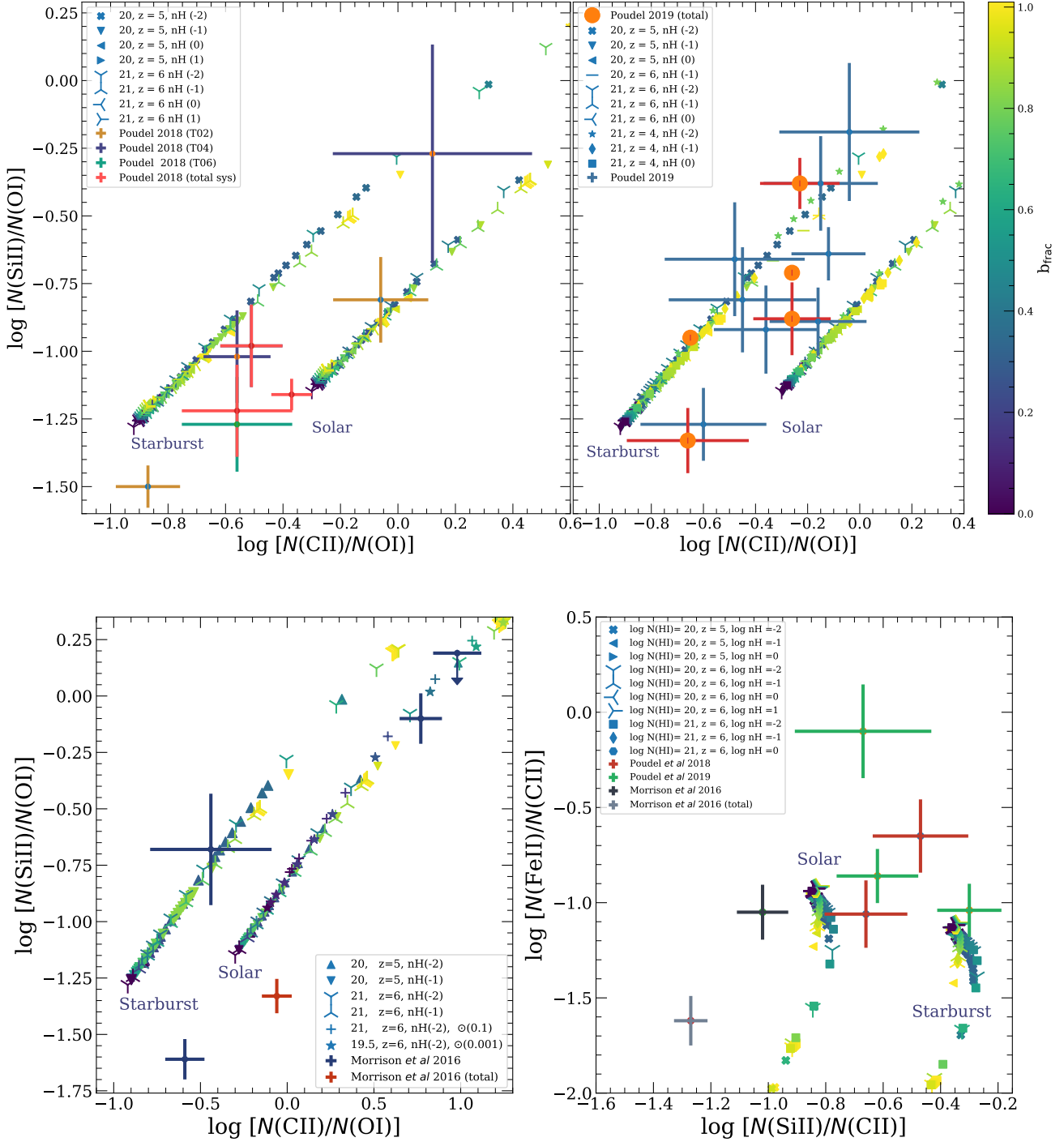


Figure 9. (Top left panel): Column density ratios of CII to OI vs SiII to OI. Data from Poudel et al. (2018). Red crosses indicate absorption complexes; blue crosses are for individual sub-components. Cloud models using CLOUDY are also shown, with the legends listing $\log N(\text{H})$ of the corresponding slab model, the redshift of the UVB model, and the surface hydrogen density. (Top right panel): Column density ratios for ion CII to OI vs SiII vs OI. The blue points/crosses correspond to distinct sub-components observed at $z > 4.5$. The orange points/red crosses are the total systems. Data taken from Poudel et al. (2019). Results for CLOUDY models are also shown. (Bottom left panel): Column density ratios for SiII to OI vs CII to OI. Data from Morrison et al. (2016). Red marker is a total system. The system on the top right is for an upper limit on SiII. (Bottom right panel): Column density ratios for FeII to CII vs SiII to CII. These are the total systems for data from both Poudel et al. (2018) and Poudel et al. (2019). We have included one individual sub-component and a total system from Morrison et al. (2016). For all panels, the colours for the CLOUDY models indicate the impact parameter of the line of sight, as indicated by the colour bars. The value $b_{\text{frac}} = 0$ recovers the slab models.

Table 4. Top table: Column densities and their ratios (both expressed as log), for representative ionisation models using CLOUDY to model the data in Fig. 9 from Poudel et al. (2018) and Poudel et al. (2019). Bottom panel: Physical properties and parameters for the models: hydrogen density (n_{H}) in cm^{-3} , pressure (P) in dyne cm^{-2} , Jeans length (λ_{J}) in kpc, radius of the cloud (R_{c}) in kpc, mass of the cloud (M_{c}) in M_{\odot} , impact parameter (b_{\perp}) in kpc, b_{frac} , model radiation field redshift, abundance and input HI density for CLOUDY ($\log N(\text{HI})$). The abundance column indicates starburst abundances (Sb) or solar abundances (\odot). (The metal column densities are normalised to $0.001Z_{\odot, S_i}$ for both solar and starburst abundance models.)

Model	HI	CII	OI	SiII	FeII	CII/OI	SiII/OI	FeII/CII	SiII/CII
1	19.03	12.77	12.88	12.48	11.36	-0.11	-0.39	-1.41	-0.28
2	20.16	13.19	13.98	12.85	11.99	-0.79	-1.13	-1.19	-0.34
3	19.95	12.93	13.78	12.58	11.78	-0.84	-1.20	-1.14	-0.35
4	20.26	13.18	14.08	12.82	12.04	-0.89	-1.25	-1.13	-0.35
5	20.30	13.22	14.12	12.86	12.08	-0.89	-1.25	-1.13	-0.35
6	20.30	13.78	13.99	12.94	12.79	-0.21	-1.05	-0.99	-0.84
7	19.71	13.45	13.42	12.64	12.38	0.03	-0.78	-1.07	-0.81
8	19.90	13.54	13.61	12.71	12.49	-0.07	-0.90	-1.04	-0.82
9	20.04	13.49	13.73	12.64	12.53	-0.24	-1.09	-0.95	-0.84
10	20.26	13.67	13.95	12.83	12.73	-0.27	-1.12	-0.94	-0.84
11	19.41	12.83	13.27	12.54	11.57	-0.44	-0.72	-1.25	-0.28
12	20.31	13.28	14.13	12.94	12.12	-0.84	-1.19	-1.16	-0.34
13	19.19	12.34	13.04	12.01	11.19	-0.69	-1.03	-1.15	-0.33
14	19.60	12.58	13.43	12.23	11.44	-0.84	-1.19	-1.14	-0.35

Model	n_{H}	$\log P$	λ_{J}	R_{c}	$\log M_{\text{c}}$	b_{\perp}	b_{frac}	redshift	abundance	$\log N(\text{HI})$
1	0.01	-13.35	11.71	2.83	7.96	0.97	0.34	5	Sb	20
2	0.01	-13.35	11.71	2.83	7.96	0.53	0.18	5	Sb	20
3	0.1	-12.47	3.28	0.12	4.93	0.08	0.67	5	Sb	20
4	0.1	-12.47	3.28	0.12	4.93	0.03	0.29	5	Sb	20
5	0.1	-12.47	3.28	0.12	4.93	0.00	0.00	5	Sb	20
6	0.01	-13.34	11.72	2.77	7.93	0.00	0.00	5	\odot	20
7	0.01	-13.34	11.72	2.77	7.93	0.78	0.28	5	\odot	20
8	0.01	-13.34	11.72	2.77	7.93	0.72	0.26	5	\odot	20
9	0.1	-12.46	3.28	0.12	4.91	0.07	0.62	5	\odot	20
10	0.1	-12.46	3.28	0.12	4.91	0.03	0.29	5	\odot	20
11	0.01	-13.38	11.43	2.24	7.77	1.14	0.51	6	Sb	21
12	0.01	-13.38	11.43	2.24	7.77	0.69	0.31	6	Sb	21
13	0.1	-12.50	3.23	0.04	3.58	0.02	0.63	6	Sb	21
14	0.1	-12.50	3.23	0.04	3.58	0.01	0.32	6	Sb	21

cloud. The absorption complex illustrates that insufficient resolution may obscure distinct physical differences in sub-components.

The absorption system at $z_{\text{abs}} = 4.809$ (purple points; data from Table 4 in Poudel et al. 2018) is matched by the models as well as its parent total system, which differs little from the sub-component with the smaller error bars. This latter is best fit by a model with starburst abundances. The other component is matched by both starburst and solar abundances, but for a line of sight well offset from the cloud centre, although the error bars are large.

Finally, both solar and starburst abundance models are consistent with the system at $z_{\text{abs}} = 4.829$ (green point; taken from Table 6 in Poudel et al. 2018) because of its large error bars. The SiII to OI ratio prefers lines of sight passing through or near a cloud centre.

The top-right panel in Fig. 9 shows the column density ratios for CII to OI vs SiII to OI from Poudel et al. (2019) (a summary of the data is in A4). As for the data of Poudel et al. (2018), metal absorption complexes are Voigt-profile fit with sub-components. We note that the absorption systems at $z_{\text{abs}} < 4.8$ were observed at much higher spectral resolution than the higher redshift absorbers or any of the systems

in Poudel et al. (2018). We model the data using the same metallicity models described above for Poudel et al. (2018) (Table 4).

The models with starburst abundances generally better match the data than solar abundances models for the resolved metal sub-components. Lines of sight passing through the centres of the clouds, however, are often in poor agreement with the data, although lines of sight passing through the inner third of the lower HI column density cloud models are acceptable. Alternatively, they may arise from lines of sight passing through the outer half of a high density model (such as Model 9 in Table 4). The ratios based on the total metal column densities are more ambiguous regarding the abundances. Only the system at $z_{\text{abs}} = 4.987$ gives a clear preference for starburst abundances. Two other systems (shown as points without error bars) are indeterminate, as the total column densities are provided as formal lower limits.

Results for the sub-DLA system at $z_{\text{abs}} = 4.98$ from Morrison et al. (2016) is shown in the bottom left panel in Fig. 9. Using the total metal column densities for the system strongly favours solar abundances, but requires silicon depletion at a level 0.15–0.4 dex. The sub-components from Voigt-

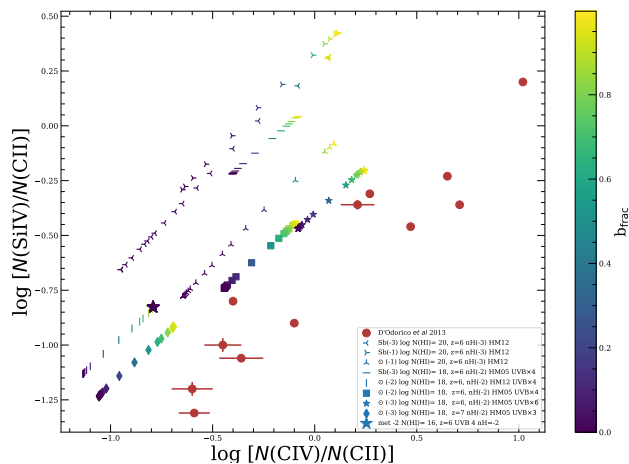


Figure 10. Column density ratios of CIV to CII vs SiIV to CII. Measurements are from D’Odorico et al. (2013). Ionisation models using CLOUDY are indicated by the coloured markers. The colour indicates the impact parameter of the line of sight for each model, as shown by the colour bar. The value $b_{\text{frac}} = 0$ recovers the slab models.

profile fitting the feature, however, are more ambiguous regarding the abundances. Only one sub-component clearly favours solar abundances, and also requires the line of sight to pass outside a cloud core. A second lies between solar and starburst abundances and is consistent with both, but the SiIII to OI ratio requires substantial depletion by 0.3–0.4 dex. The depletion analysis by Morrison et al. (2016) confirms this as a high depletion system. A third sub-component favours starburst abundances, but its large error bars permit consistency with solar as well. The complex also has detected CIV and SiIV absorption, but given the small errors on the redshifts of the sub-components ($\Delta z_{\text{abs}} < 10^{-4}$), it is unclear these sub-components should be associated with the low-ionisation sub-components, or to which sub-component, so we refrain from comparisons with the models.

The bottom right panel in Fig. 9 shows FeII systems. We show ratios for the total column densities of FeII to CII vs SiII to CII from absorption complexes (compiled from both Poudel et al. 2018, 2019). The data for individual sub-components for FeII is incomplete, with FeII undetected in any sub-component in the Poudel et al. (2018) data for which OI, CII or SiII was detected. Only one sub-component, at $z_{\text{abs}} = 5.05024$, in the data from Poudel et al. (2019) had a detection in all three of CII, SiII and FeII. Given the large errors, the data are generally consistent with either solar or starburst abundances, for lines of sight passing preferentially through the cloud centres, but the data do have generally high values of FeII to CII, especially the system at $z_{\text{abs}} = 4.589$. The sub-DLA at $z_{\text{abs}} = 4.98$ from Morrison et al. (2016), however, now clearly favours solar abundances, with a silicon depletion factor relative to carbon of $\sim 0.3 - 0.5$ dex.

Because the metals in the outer layers of sub-DLA and DLA systems may exist in high ionisation states, we also model the high redshift data for high ionisation absorbers from D’Odorico et al. (2013). Column density ratios between for CIV, SiIV and CII detected at $5 < z < 6$ are shown in Fig. 10. These measurements were taken using the X-Shooter

spectrograph with resolution between 27 - 53 km s $^{-1}$. The signal-to-noise ratios (SNRs), computed for each resolution element, range over $7 < \text{SNR} < 125$. (See Table 5 for details.)

Isobaric cloud models using CLOUDY do not provide good matches to these systems, as shown in Fig. 10, but lie systematically offset from the trends. The offset may arise either because of a low silicon to carbon ratio in the observed systems, with depletion factors up to ~ 0.5 dex, or from too low ionisation. Models that best approximate the column densities in these systems use a radiation field from the HM05 table in CLOUDY, which enhances the ultraviolet background contribution from quasars compared with the model of Haardt & Madau (2012). (See the CLOUDY documentation for details.) For isobaric models with $\log N(\text{HI})=20$ to come near to reproducing the measured values, the hydrogen density at the surface must exceed $n_{\text{H}} > 0.001 \text{ cm}^{-3}$ with $R_{\text{c}} > \lambda_{\text{J}}$ (see table 5), and so are Jeans unstable. We explored alternative values for the HI column densities from $\log N(\text{HI}) = 16$ to 21 cm^{-2} . The best fitting models are for lines of sight passing through the outer regions of the clouds with low central HI column densities of 10^{18} cm^{-2} , similar to the slab models in D’Odorico et al. (2013). Some of the data points still extend to higher ratios of SiIV to CII (and CIV to CII) than predicted by the models.

Models with solar abundances, and metallicities between 0.001- 0.01 Z_{\odot} , are more consistent with the observations than models with starburst abundances. We also found that, even using the HM05 radiation field, further boosting in the intensity was required, as may be provided by local radiation sources. Examples with boost factors of 3, 4 and 6 are shown. Similar conclusions were reached by D’Odorico et al. (2013). Few, if any, of the observed systems appear to arise from the outer regions of pressure-confined sub-DLAs or DLAs.

For completeness, we also looked at the early data of two low-ionisation systems (showing AlII, FeII and in one case SiII) detected in the spectra of QSOs at $z_{\text{abs}} > 5$ (Ryan-Weber et al. 2009). (Six other systems at $z > 5$ show only CIV.) The measurements were taken with NIRSPEC on the Keck II telescope and with ISAAC on the VLT-UT1, with a $\text{SNR} \gtrsim 5$. A summary of the observations is provided in the top panel of Table 6. The reported equivalent widths were converted to column densities using the atomic data from Morton (1991). The bottom panel shows the physical properties of representative models for the clouds. For the system at $z_{\text{abs}} = 5.594$ in the spectrum of J084035.09+562419.9, the models struggle to reproduce the measured ratio $\log[N(\text{SiII})/N(\text{FeII})] = -0.34$. As uncertainties on the measurements are not provided, we cannot estimate the degree of discrepancy between the models and the measurements. The closest model we find is $\log[N(\text{SiII})/N(\text{FeII})] = 0.09$ (fifth model in Table 6), corresponding to a small cloud ($R_{\text{c}} \approx 5 \text{ pc}$) with high hydrogen density and with a mass of $\sim 13 M_{\odot}$, well below the thermal evaporation mass limit. Models match the measured value $\log[N(\text{SiII})/N(\text{AlII})] \approx 1.06$, such as a cloud with $R_{\text{c}} \approx 160 \text{ pc}$ and mass $\sim 4.1 \times 10^4 M_{\odot}$. The measured value $\log[N(\text{FeII})/N(\text{AlII})] = 1.4$ was not matched by the models. Values above 0.94 require very small cloud sizes, below $\sim 20 \text{ pc}$, with high hydrogen densities and masses below the thermal evaporation limit. The HI column densities for the models best matching the data correspond to sub-

Table 5. Summary of the physical properties and parameters for models of the data from D’Odorico et al. (2013). Listed are the hydrogen density (n_{H}) in cm^{-3} , pressure (P) in dyne cm^{-2} , Jeans length (λ_{J}) in kpc, cloud radius (R_{c}) in kpc, cloud mass (M_{c}) in M_{\odot} and parameter values for the ionisation models: redshift of UV background model, chemical abundance and metallicity, and HI column densities, for models shown in Fig. 10.

$\log n_{\text{H}}$	$\log P$	λ_{J}	R_{c}	$\log M_{\text{c}}$	z	Ab, Z/Z_{\odot}	$\log N(\text{HI})$
-3.00	-14.25	41.78	149.94	11.89	6	Sb 0.001	20
-2.00	-13.38	11.43	2.04	7.61	6	Sb 0.001	20
-3.00	-14.32	38.19	136.78	11.63	6	\odot 0.1	20
-2.00	-13.41	11.03	1.34	6.75	6	\odot 0.1	20
-3.00	-14.04	52.85	785.48	13.97	6 UVB \times 4	Sb 0.001	18
-2.00	-13.27	12.97	8.22	8.94	6 UVB \times 4	Sb 0.001	18
-3.00	-14.17	45.51	581.34	13.48	6 UVB \times 4	\odot 0.01	18
-2.00	-13.30	12.37	4.50	8.15	6 UVB \times 4	\odot 0.01	18
-3.00	-14.04	52.27	703.18	13.83	6 HM05 UVB 4	\odot 0.01	18
-2.00	-13.26	12.91	7.98	8.90	6 HM05 UVB 4	\odot 0.01	18
-3.00	-14.11	48.66	467.92	13.26	7 HM05 UVB 3	\odot 0.001	18
-2.00	-13.29	12.44	4.37	8.11	7 HM05 UVB 3	\odot 0.001	18

Table 6. Top table: Column densities for SiII, FeII and AlII obtained using the equivalent width measurements (W_0) [\AA] of unsaturated lines from Ryan-Weber et al. (2009). Bottom table: Estimated values for the same ions, column density ratios and their physical properties from photoionisation models for isobaric clouds using CLOUDY. We take as a reference the calculated column density ratios for J084035.09+562419.9 $\log[N(\text{SiII})/N(\text{FeII})] = -0.34$, $\log[N(\text{SiII})/N(\text{AlII})] = 1.05$, $\log[N(\text{FeII})/N(\text{AlII})] = 1.39$. For the object J113717.73+354956.9 $\log[N(\text{FeII})/N(\text{AlII})] = 1.47$. Listed are the hydrogen density (n_{H}) in cm^{-3} , pressure (P) in dyne cm^{-2} , Jeans length (λ_{J}) in kpc, cloud radius (R_{c}) in kpc, cloud mass (M_{c}) in M_{\odot} , impact parameter (b_{\perp}) in kpc and $b_{\text{frac}} = b_{\perp}/R_{\text{c}}$ for isobaric cloud models. All models assume a UV background at $z = 6$ from Haardt & Madau (2012) and solar abundances with $Z = 0.1Z_{\odot}$. (All column densities and their ratios are expressed as \log .)

SDSS QSO name	z_{abs}	λ	W_0	$\log \lambda f$	$\log N(\text{SiII})$	$\log N(\text{Fe II})$	$\log N(\text{Al II})$
J084035.09+562419.9	5.5940	1526.70698	0.52	2.546	14.039
	5.5938	1608.45085	0.34	1.998	...	14.38	...
	5.5943	1670.7886	0.44	3.486	12.98
J113717.73+354956.9	5.0120	1608.45085	0.65	1.998	...	14.66	...
	5.0127	1670.7886	0.7	3.486	13.18

HI	SiII	AlII	FeII	$\frac{\text{SiII}}{\text{FeII}}$	$\frac{\text{SiII}}{\text{AlII}}$	$\frac{\text{FeII}}{\text{AlII}}$	$\log n_{\text{H}}$	$\log P$	λ_{J}	R_{c}	$\log M_{\text{c}}$	b_{\perp}	b_{frac}
18.99	14.30	13.40	13.93	0.36	0.89	0.52	-2.0	-13.40	11.03	1.34	6.75	0.2	0.15
17.76	13.48	12.57	12.97	0.50	0.90	0.40	-1.5	-12.95	5.89	0.16	4.61	0.15	0.91
19.42	14.21	13.17	14.03	0.17	1.03	0.86	-1.5	-12.95	5.89	0.16	4.61	0.0	0.0
19.21	13.94	12.87	13.81	0.12	1.06	0.94	-1.0	-12.51	3.16	0.02	2.75	0.003	0.10
19.17	13.80	12.73	13.70	0.09	1.06	0.96	-0.5	-12.09	1.70	0.005	1.12	0.0	0.0
19.54	14.59	13.83	14.22	0.37	0.76	0.38	-2.5	-13.86	20.59	12.91	9.11	0.11	0.009
19.57	14.60	13.83	14.23	0.36	0.76	0.40	-2.5	-13.86	20.59	12.91	9.11	0.0	0.0

DLAs. For the system at $z_{\text{abs}} = 5.012$ in the spectrum of J113717.73+354956.9, the measured value $\log[N(\text{Fe II})/N(\text{Al II})] \approx 0.47$, the best match is provided by clouds with larger sizes of $\sim 0.1 - 10$ kpc and masses $\sim 10^4 - 10^9 M_{\odot}$, and possibly with a HI column density smaller than 10^{19}cm^{-2} . It would be interesting to re-observe this system at higher resolution and signal-to-noise ratio, particularly to investigate possible sub-components of the features.

5 DISCUSSION

Our main goal in this paper is to interpret the metal absorption line data in sub-DLAs and DLAs at high redshift in terms of a model of clouds pressure-confined by the gas in galactic haloes to infer the properties of the stellar popu-

lations that produced the metals. As these systems arise in the first billion years of the Universe, the metals should shed light on the stellar populations of the first galaxies. Central to this goal is establishing whether the pressure-confined model is supported by the data. In this section, we discuss our findings for the pressure-confined cloud models as they relate to individual sets of observations.

For the systems observed at these redshifts by Becker et al. (2011, 2012) (Figs. 6 and 7), the models are consistent with their suggestion that the low ionisation metal systems they detected arise in DLAs. Models with $\log N(\text{HI}) = 10^{20} - 10^{21} \text{cm}^{-2}$ provide $N(\text{CII})/N(\text{OI})$ ratios consistent with their data for metal abundances between starburst and solar values and metallicities of $0.001 - 0.01Z_{\odot}$. The measured values of $N(\text{SiII})/N(\text{OI})$, however, lie systematically low by about 0.2 dex for lines of sight passing through the cloud cen-

tres. Boosting the UVB shifts the SiII to OII and CII to OII mostly along the same locus as varying the impact parameter, and away from the measured values. Depletion onto dust grains is another complicating factor for interpreting metal line ratios in DLAs and sub-DLAs. As silicon is a refractory element, the offset may arise from depletion within the cloud centres: for the low metallicities of these systems, very little depletion is expected, but 0.2 dex is consistent with the level of depletion assessed for low metallicity DLAs at moderate redshifts of $z \sim 2.5$ (Akerman et al. 2005). Depletion analyses of $z \gtrsim 5$ sub-DLAs and DLAs also support depletion levels at least as strong as at moderate redshifts for comparable metallicities (Morrison et al. 2016; Poudel et al. 2019). Allowing for this level of silicon depletion, the measured $N(\text{FeII})/N(\text{CII})$ values again broadly bridge abundances between solar and starburst values. The measured ratio $N(\text{SiII})/N(\text{FeII})$ is found enhanced over solar by about 0.25–0.45 dex. Models with enhanced UVB intensities (multiplying by factors of 2 and 4) shift the FeII to SiII ratio by only 0.05 – 0.1 dex. Since iron is also a refractory element, the larger measured shifts may be accounted for by depletion onto dust grains. As pointed out by Becker et al. (2012), the shifts are also consistent with abundance measurements for low metallicity halo stars in the Galaxy (Cayrel et al. 2004). We refer to Becker et al. (2012) and Cooke et al. (2011) for further discussion of the interpretation of metal abundances in very low metallicity DLAs.

The column density ratios for the systems measured by Poudel et al. (2018) are similar to those from the slightly higher redshift data of Becker et al. (2011, 2012), again consistent with abundances between starburst and solar. One system ($z_{\text{abs}} = 5.335$) illustrates a possible hazard in interpreting under-resolved features. Voigt-profile fitting resolves the feature into two sub-components. The total metal column densities of CII, SiII and OI are consistent with a line of sight passing through the core of a DLA with solar abundances, and inconsistent with any model with starburst abundances. The sub-components, however, tell another story. Whilst one is consistent with the solar abundance interpretation, it favours a line of sight offset from the absorber core. The CII to OI ratio for the other sub-component is inconsistent with a model having solar abundances, but is consistent with a starburst abundance interpretation. Its SiII to OI ratio is too low, but only by ~ 0.25 dex, which could indicate a small level of depletion onto dust grains. The interpretation of the sub-components is thus rather different from the interpretation the averaged column densities would suggest.

Similar behaviour is found for the sub-DLA at $z_{\text{abs}} = 4.98$ (Morrison et al. 2016). Ratios of the total metal column densities for the feature suggest a silicon depleted system with solar abundances. The feature is resolved into several sub-components, three of which have all of OI, CII and SiII detected. A highly silicon-depleted sub-component survives, but its abundance is less clear-cut, consistent with both solar and starburst abundances given the errors, as is another sub-component. The remaining, however, strongly favours starburst abundances, and moreover suggests the line of sight passes outside the core of the cloud. High spectral resolution data is clearly required to interpret complex metal absorption features, which may arise from a mixture of systems with varied chemical composition.

Compared with the systems above, whilst the abundances inferred from the OI, CII and SiII column densities measured by Poudel et al. (2019) span the range from starburst to solar, they more broadly indicate starburst abundances in the clouds. Consistency with the pressure-confined models, however, suggests the lines of sight often pass outside the cloud cores, as the predicted ratios of SiII to OI are otherwise too small. As shown in Fig. 5, the CII and SiII fractions fall away much more slowly than HI and OI for lines of sight increasingly displaced from the cloud centres. Geometry may play an important role in interpreting the metal line ratios in systems optically thick to ionising radiation.

Almost all of the absorption systems are resolved into sub-components by Voigt-profile fitting. In every case but one, when a system contains one or more sub-components with column density ratios corresponding to a line of sight consistent with passing outside a cloud core, the complex contains at least one other sub-component favouring a line of sight passing through a cloud core. The measured HI may be interpreted as arising from the latter, as the lines of sight passing outside the core may have $\log N(\text{HI}) < 20$.¹ An exception is the complex at $z_{\text{abs}} = 4.987$ in QSO J0306+1853. Poudel et al. (2019) obtain a silicon-to-oxygen ratio for the system of $[\text{Si}/\text{O}] = 0.79 \pm 0.09$, which they recognise as surprisingly high. As the QSO was observed with the lowest resolution of any of their observations ($R = 4100$), they suggest that higher resolution observations may be required to obtain more accurate column densities for the metals. Should higher resolution observations maintain the high silicon abundance, one interpretation may be that most of the measured HI arises in a near pristine cloud, with a metallicity below $0.001Z_{\odot}$, and that the high SiII to OI ratio originates from gas outside the core of a second pressure-confined cloud that has been polluted by metals (such as Model 1 in Table 4).

We note that a determination of the metallicities is less secure since the measured HI column densities are strictly upper limits to the metal systems since the Lyman α and Lyman β (when available) absorption features alone are broader than the velocity separation between metal sub-components in a complex. Without higher order Lyman series measurements to isolate the redshift of HI absorption corresponding to the metal features, the HI column density to assign to each sub-component is unclear. We find models with metallicities $0.001 - 0.01Z_{\odot}$ provide good matches to the data. When FeII measurements are available, the metallicities are closer to $0.01Z_{\odot}$. Poudel et al. (2019) infer metallicities somewhat above $0.01Z_{\odot}$ for some systems, but do not allow for an ionisation correction to the measured HI column density. For a line of sight passing outside the core of a cloud, Fig. 5 shows the ionisation corrections may be substantial, as much as an order of magnitude or larger for HI than for CII and SiII. On the other hand, the correction for oxygen is comparable to that for hydrogen (since

¹ An alternative interpretation of column density ratios that do not correspond to the predictions for the core of a DLA or sub-DLA, where they are largely shielded from the metagalactic photoionising radiation field, is that they arise from lower HI column density systems that need not be pressure confined. Our point is the pressure-confined models may be able to explain the column density ratios for these absorption systems as well.

the ionisation potentials are nearly the same), so that the ratio of OI to HI should be a good indicator of the metallicity, although it will be abundance-dependent if referenced to iron, which is 0.8 dex less abundant for starburst abundances than solar for the same oxygen abundance (see Table 2). The anomalously high iron abundance for the system at $z_{\text{abs}} = 4.589$ of $Z_{\text{Fe}} \approx 0.1Z_{\odot}$ is difficult to accommodate in any model, especially as it appears in a sub-component without other detected metal absorption based on the Voigt-profile fit to the overall feature, which was resolved into two sub-components. Poudel et al. (2019) note the iron feature is blue-shifted relative to the other metal features, which may indicate local iron-enriched material in an outflow from a Type Ia supernova. A system measured by Ryan-Weber et al. (2009) (at $z_{\text{abs}} = 5.594$) similarly shows an anomalously high iron abundance the models are unable to match.

We also examined the possibility that some of the high ionisation absorption systems, including CIV and SiIV, reported by D’Odorico et al. (2013) may arise in the outer layers of pressure-confined sub-DLA or DLA systems. The column density ratios do not support the possibility: the systems appear generally to have HI column densities of around 10^{18} cm^{-2} .

6 CONCLUSIONS

The metal absorption lines measured in sub-DLA and DLA systems at $z \gtrsim 5$ may provide important clues to the origin and nature of galaxies in the first billion years in the Universe. We analysed measurements reported in the literature of sub-DLA and DLA systems to test the possibility that such systems arise from pressure-confined clouds in galactic haloes, and interpret the measurements in the context of this model to infer the physical properties of the clouds. To do so, we extended simple slab models for sub-DLAs and DLAs to allow for lines of sight that pass outside the largely neutral hydrogen cores of the clouds. We approximated the clouds by rolling slab models computed using CLOUDY into cylinders, which should capture the main effects of ionisation layers in a spherical pressure-confined cloud on the metal column density ratios for off-centre lines of sight. Using this procedure, we found pressure-confined clouds provide a viable model for low-ionisation intervening metal absorption systems approaching the epoch of reionization.

We reached the following specific conclusions:

- Typical gas densities, pressures, sizes and masses of acceptable model clouds range over, respectively, $0.01 \lesssim n_{\text{H}} \lesssim 0.1 \text{ cm}^{-3}$, $-14.2 < \log P[\text{dyne cm}^{-2}] < -12.5$, $0.04 < R_c < 3 \text{ kpc}$ and $3.5 < \log M_c/M_{\odot} < 8$. The cloud pressures are consistent with expectations for virialized regions of dark matter haloes at $5 \lesssim z \lesssim 6$ with masses $11 < \log M_h/h^{-1}M_{\odot} < 12$. The gas densities must exceed $n_{\text{H}} > 0.001 \text{ cm}^{-3}$ for the clouds to be Jeans stable.

- The best-fitting models have typical HI column densities consistent with sub-DLAs ($10^{19} - 10^{20.3} \text{ cm}^{-2}$) and DLAs ($> 10^{20.3} \text{ cm}^{-2}$), with metallicities $0.001 - 0.01Z_{\odot}$.

- The best-fitting models have metal abundances that range between α -enhanced abundances expected for a stellar population dominated by massive stars (starburst abundances based on a chemical evolution model from Hamann &

Ferland 1993, with a top-heavy stellar initial mass function) and solar abundances.

- The best-fitting model inferred from the ratios between total metal column densities in an absorption complex can differ qualitatively from the models that best fit the individual sub-components, emphasising the need for high resolution, high signal-to-noise ratio data.

- The model predicts that any sub-component arising from a line of sight offset from the core of a cloud should be accompanied by at least one sub-component arising from a line of sight passing through a cloud core to account for the high HI column density. This is found generally borne out by the data.

- Models of the two proximate DLAs (D’Odorico et al. 2018; Bañados et al. 2019) examined favour solar abundances, although the systems are too few to draw a general conclusion.

- Variations in the UVB have a moderate effect on the metal ion column densities, but primarily for lines-of-sight in the outer regions of the clouds where the absorption of HI or OI ionising radiation is reduced. The shifts in the column densities of singly ionised species is only about 0.05–0.1 dex.

The masses and radii estimated for the pressure-confined systems reproducing the metal absorption data make it challenging to study the clouds using cosmological hydro-simulations. Recent simulations exploring the impact spatial and mass resolution has on the modelling of gas clouds and filaments in galaxy scale simulations are just beginning to reach the scales of the moderately sized clouds, but resolving scales down to 10 pc is still beyond their capacity (eg Peebles et al. 2019; van de Voort et al. 2019). Resolving the sizes of low-ionisation metal species is especially difficult. Establishing the relation of low-ionisation clouds to galaxy formation must continue to await further improvements in the numerical simulations. Until then, analytic models provide a helpful means of interpreting the growing amount of data.

ACKNOWLEDGEMENTS

TS and AM gratefully acknowledge support from the UK Science and Technology Facilities Council, Consolidate Grant ST/R000972/1. TS thanks Juan V. Hernández for useful coding comments. This research also made use of ASTROPY, a community-developed core PYTHON package for Astronomy (Astropy Collaboration et al. 2013) and MATPLOTLIB (Hunter, J. D. 2007).

DATA AVAILABILITY

The data underlying this article will be shared on reasonable request to the corresponding author.

REFERENCES

- Akerman C. J., Ellison S. L., Pettini M., Steidel C. C., 2005, *A&A*, **440**, 499
 Armillotta L., Fraternali F., Werk J. K., Prochaska J. X., Marinacci F., 2017, *MNRAS*, **470**, 114

- Astropy Collaboration et al., 2013, *A&A*, 558, A33
- Bañados E., et al., 2019, *ApJ*, 885, 59
- Barnes L. A., Haehnelt M. G., 2014, *MNRAS*, 440, 2313
- Becker G. D., Sargent W. L. W., Rauch M., Calverley A. P., 2011, *ApJ*, 735, 93
- Becker G. D., Sargent W. L. W., Rauch M., Carswell R. F., 2012, *ApJ*, 744, 91
- Becker G. D., Bolton J. S., Madau P., Pettini M., Ryan-Weber E. V., Venemans B. P., 2015, *MNRAS*, 447, 3402
- Bolton J. S., Puchwein E., Sijacki D., Haehnelt M. G., Kim T.-S., Meiksin A., Regan J. A., Viel M., 2017, *MNRAS*, 464, 897
- Bosman S. E. I., Fan X., Jiang L., Reed S., Matsuoka Y., Becker G., Haehnelt M., 2018, *MNRAS*, 479, 1055
- Bouwens R. J., Illingworth G. D., Oesch P. A., Caruana J., Holwerda B., Smit R., Wilkins S., 2015, *ApJ*, 811, 140
- Cayrel R., et al., 2004, *A&A*, 416, 1117
- Chambers K. C., et al., 2016, arXiv e-prints, p. arXiv:1612.05560
- Christlieb N., et al., 2002, *Nature*, 419, 904
- Cooke R., Pettini M., Steidel C. C., Rudie G. C., Nissen P. E., 2011, *MNRAS*, 417, 1534
- Cooke R. J., Pettini M., Jorgenson R. A., 2015, *ApJ*, 800, 12
- D’Odorico V., et al., 2013, *MNRAS*, 435, 1198
- D’Odorico V., et al., 2018, *The Astrophysical Journal*, 863, L29
- Davies F. B., et al., 2018, *ApJ*, 864, 142
- Ellison S. L., Prochaska J. X., Hennawi J., Lopez S., Usher C., Wolfe A. M., Russell D. M., Benn C. R., 2010, *MNRAS*, 406, 1435
- Ferland G. J., Korista K. T., Verner D. A., Ferguson J. W., Kingdon J. B., Verner E. M., 1998, *PASP*, 110, 761
- Ferland G. J., et al., 2017, *Rev. Mex. Astron. Astrofis.*, 53, 385
- Finkelstein S. L., et al., 2019, *ApJ*, 879, 36
- Font-Ribera A., et al., 2012, *J. Cosmology Astropart. Phys.*, 2012, 059
- Frebel A., et al., 2005, *Nature*, 434, 871
- Frebel A., Johnson J. L., Bromm V., 2007, *MNRAS*, 380, L40
- Giallongo E., et al., 2015, *A&A*, 578, A83
- Greig B., Mesinger A., Haiman Z., Simcoe R. A., 2017, *MNRAS*, 466, 4239
- Haardt F., Madau P., 2012, *ApJ*, 746, 125
- Hamann F., Ferland G., 1993, *ApJ*, 418, 11
- Hunter, J. D. 2007, *Computing In Science & Engineering*, 9, 90
- Lan T.-W., Fukugita M., 2017, *ApJ*, 850, 156
- Lan T.-W., Mo H., 2019, *MNRAS*, 486, 608
- Mason C. A., Treu T., Dijkstra M., Mesinger A., Trenti M., Pennericci L., de Barros S., Vanzella E., 2018, *ApJ*, 856, 2
- McQuinn M., 2016, *Annual Review of Astronomy and Astrophysics*, 54, 313
- Meiksin A., Bolton J. S., Puchwein E., 2017, *MNRAS*, 468, 1893
- Mo H. J., Miralda-Escude J., 1996, *ApJ*, 469, 589
- Morrison S., Kulkarni V. P., Som D., DeMarcy B., Quiret S., Péroux C., 2016, *ApJ*, 830, 158
- Morton D. C., 1991, *ApJS*, 77, 119
- Norris J. E., Christlieb N., Korn A. J., Eriksson K., Bessell M. S., Beers T. C., Wisotzki L., Reimers D., 2007, *ApJ*, 670, 774
- Oppenheimer B. D., Davé R., Katz N., Kollmeier J. A., Weinberg D. H., 2012, *MNRAS*, 420, 829
- Peeples M. S., et al., 2019, *ApJ*, 873, 129
- Pettini M., Smith L. J., King D. L., Hunstead R. W., 1997, *ApJ*, 486, 665
- Planck Collaboration 2018, preprint, (arXiv:1807.06209)
- Poudel S., Kulkarni V. P., Morrison S., Péroux C., Som D., Rahmani H., Quiret S., 2018, *MNRAS*, 473, 3559
- Poudel S., Kulkarni V. P., Cashman F. H., Frye B., Péroux C., Rahmani H., Quiret S., 2019, *MNRAS*, p. 2603
- Prochaska J. X., Hennawi J. F., 2009, *ApJ*, 690, 1558
- Prochaska J. X., Gawiser E., Wolfe A. M., Cooke J., Gelino D., 2003, *ApJS*, 147, 227
- Puchwein E., Springel V., 2013, *MNRAS*, 428, 2966
- Puchwein E., Haardt F., Haehnelt M. G., Madau P., 2019, *MNRAS*, 485, 47
- Rafelski M., Wolfe A. M., Prochaska J. X., Neeleman M., Mendez A. J., 2012, *ApJ*, 755, 89
- Rao S. M., Prochaska J. X., Howk J. C., Wolfe A. M., 2005, *AJ*, 129, 9
- Ryan-Weber E. V., Pettini M., Madau P., Zych B. J., 2009, *MNRAS*, 395, 1476
- Segers M. C., Schaye J., Bower R. G., Crain R. A., Schaller M., Theuns T., 2016, *MNRAS*, 461, L102
- Somerville R. S., Davé R., 2015, *ARA&A*, 53, 51
- Sparre M., Pfrommer C., Vogelsberger M., 2019, *MNRAS*, 482, 5401
- Spitzer L., 1978, *Physical processes in the interstellar medium*. Wiley VCH, doi:10.1002/9783527617722
- Starkenburg E., Oman K. A., Navarro J. F., Crain R. A., Fattahi A., Frenk C. S., Sawala T., Schaye J., 2016, *Monthly Notices of the Royal Astronomical Society*, 465, 2212
- Suarez T., Pontzen A., Peiris H. V., Slyz A., Devriendt J., 2016, *MNRAS*, 462, 994
- Suresh J., Bird S., Vogelsberger M., Genel S., Torrey P., Sijacki D., Springel V., Hernquist L., 2015, *MNRAS*, 448, 895
- Tumlinson J., Peebles M. S., Werk J. K., 2017, *ARA&A*, 55, 389
- Turner M. L., Schaye J., Crain R. A., Rudie G., Steidel C. C., Strom A., Theuns T., 2017, *MNRAS*, 471, 690
- Wolfe A. M., Gawiser E., Prochaska J. X., 2005, *ARA&A*, 43, 861
- van de Voort F., Springel V., Mandelker N., van den Bosch F. C., Pakmor R., 2019, *MNRAS*, 482, L85

APPENDIX A: TABLES

In this section, tables are provided of the data used for the figures taken from Becker et al. (2011), Becker et al. (2012), Morrison et al. (2016), Poudel et al. (2018) and Poudel et al. (2019), D’Odorico et al. (2013) and Bañados et al. (2019).

This paper has been typeset from a $\text{\TeX}/\text{\LaTeX}$ file prepared by the author.

Table A1. Data from [Becker et al. \(2011, 2012\)](#)

SDSS QSO name	z_{abs}	$\log N_{\text{OI}}$	$\log N_{\text{CII}}$	$\log N_{\text{SiII}}$	$\log N_{\text{FeII}}$	$\log N_{\text{CIV}}$	$\log N_{\text{SiIV}}$
J0040-0915	4.7393	> 15.0	>14.6	14.13±0.02	13.77±0.06
J1208+0010	5.0817	> 14.7	>14.3	13.75±0.03	13.27±0.07
J0231-0728	5.338	14.47±0.05	13.79±0.05	13.15±0.04	12.73±0.04
		...	14.13±0.04	13.42±0.02	12.94±0.05
J0818+1722	5.7911	14.54±0.03	14.13±0.03	13.36±0.04	12.89±0.07
		...	14.19±0.03	13.41±0.03	12.95±0.07	<13.4	<12.9
J0818+1722	5.8765	14.04±0.05	13.62±0.07	12.78±0.05	<12.7	<13.0	<12.6
J1623+3112	5.8415	>15.0	>14.3	14.09±0.02	<13.0
J1148+5251	6.0115	14.65±0.02	14.14±0.06	13.51±0.03	13.21±0.25	<13.8	<12.7
J1148+5251	6.1312	14.79±0.23	13.88±0.15	13.29±0.06	13.03±0.18	<13.2	<12.3
J1148+5251	6.1988	13.49±0.13	12.90±0.11	12.12±0.05	...	<13.6	<12.9
J1148+5251	6.2575	14.12±0.15	13.78±0.21	12.92±0.08	<12.7	...	<12.5

Table A2. Data from [Morrison et al. \(2016\)](#).

SDSS QSO name	z_{abs}	z	$\log N_{\text{HI}}$	$\log N_{\text{OI}}$	$\log N_{\text{CII}}$	$\log N_{\text{SiII}}$	$\log N_{\text{FeII}}$
Q1202+3235	$z = 4.977$	4.977004±0.000002	...	14.50±0.08	13.91±0.08	12.89±0.04	12.86±0.12
		4.977259±0.000009	...	13.07±0.21	12.63± 0.28	12.39±0.13	...
		4.978517±0.000008	...	12.89±0.10	13.66± 0.07	12.79±0.05	...
		4.978761±0.000008	...	13.02±0.07	14.00± 0.12
		Total log N	19.83±0.10	14.54±0.07	14.48±0.05	13.21±0.03	12.86±0.12

Table A3. Data from [Poudel et al. \(2018\)](#).

SDSS QSO name	z_{abs}	z	$\log N_{\text{HI}}$	$\log N_{\text{OI}}$	$\log N_{\text{CII}}$	$\log N_{\text{SiII}}$	$\log N_{\text{FeII}}$
Q0231-0728	$z = 5.335$	5.33505±0.00003	...	14.41±0.05	13.54±0.10	12.91±0.06	...
		5.33636±0.00015	...	13.89±0.15	13.83± 0.07	13.08±0.05	...
		Total log N	20.10±0.15	14.55±0.05	14.18±0.05	13.39±0.03	...
Q0824+1302	$z = 4.809$	4.80253±0.00013	...	13.01±0.29	13.13±0.19	12.74±0.28	...
		4.80922±0.00003	...	14.18±0.06	13.62±0.10	13.16±0.16	...
		Total log N	20.10±0.15	14.28±0.06	13.77±0.09	13.30±0.14	13.12±0.17
Q0824+1302	$z = 4.829$	4.82908±0.00002	...	15.44±0.15	14.88±0.12	14.17±0.09	...
		Total log N	20.80±0.15	15.44±0.15	14.88±0.12	14.22±0.08	13.82±0.13

Table A4. Data from Table 2 of Poudel et al. (2019).

SDSS QSO name	z_{abs}	z	$\log N_{\text{HI}}$	$\log N_{\text{OI}}$	$\log N_{\text{CII}}$	$\log N_{\text{SIII}}$	$\log N_{\text{FeII}}$
J0306+1853	4.987	4.98661±0.00004	...	14.28±0.16	14.13±0.15	13.9±0.07	...
		Total log N	20.60±0.15	14.60±0.08	14.37±0.13	14.22±0.05	...
J1233+0622	4.859	4.85795±0.00004	...	> 15.30	14.42±0.07	13.82±0.19	...
		Total log N	20.75±0.15	>15.30	14.74±0.05	14.35 ± 0.10	13.61±0.13
J1233+0622*	5.050	5.05024±0.00001	...	15.11±0.12	14.75±0.16	14.19±0.11	14.07±0.09
		5.05188±0.00004	...	13.88±0.19	13.84±0.19	13.69±0.17	...
		Total log N	20.10±0.15	15.19 ± 0.10	14.93 ± 0.11	14.31 ± 0.09	14.07 ± 0.09
J1253+1046	4.589	4.58916±0.00005	13.89±0.17
		4.58948±0.00004	...	14.94±0.10	14.34±0.22	13.67±0.09	...
		Total log N	19.75±0.15	15.00 ± 0.08	14.34 ± 0.22	13.67 ± 0.09	14.24 ± 0.11
	4.600	4.60003±0.00003	...	15.53±0.08	14.78±0.20	14.57±0.05	...
		Total log N	20.35±0.15	> 15.58	> 14.78	14.57±0.05	14.06 ± 0.29
J1557+1018	4.627	4.62512±0.00004	...	14.54±0.11	14.38±0.15	13.65±0.06	...
		4.62694±0.00002	...	15.64±0.09	15.52±0.11	15.00±0.04	...
		4.62885±0.00003	...	15.55±0.19	15.10±0.21	14.74±0.04	...
		4.63018±0.00015	...	15.01±0.19	14.53±0.19	14.35±0.09	...
		Total log N	20.75±0.15	> 15.97	> 15.71	> 15.26	...

Table A5. Data from D'Odorico et al. (2013).

SDSS QSO name	z_{abs}	$\log N_{\text{CII}}$	$\log N_{\text{CIV}}$	$\log N_{\text{SiIV}}$
SDSSJ0818+1722	5.7899±0.0002	...	13.2±0.1	< 12.5
	5.78909±0.00004	13.56±0.04
	5.8441±0.0001	> 13.0	13.27±0.07	12.69±0.06
	5.8770±0.0001	...	13.22±0.07	<12.5
	5.87644±00002	13.81±0.03
SDSSJ0836+0054	5.32277±0.00004	<13.0	13.65±0.04	12.77±0.04
SDSSJ1030+0524	5.72419±0.0001	<13.5	14.52±0.08	<13.7
	5.74116±0.00004	...	13.8±0.1	13.20±0.03
	5.74097±0.00001	14.40±0.01
	5.7440±0.0002	...	13.89±0.09	...
	5.74425±0.00004	13.34±0.03
	5.74399±0.00004	14.34±0.01
	5.9757±0.0004	<13.5	13.1±0.3	<12.7
	5.9784±0.0002	...	13.4±0.2	...
5.97896±0.00009	<13.5	...	12.6±0.1	
SDSSJI319+0950	5.57049±0.00003	<13.5	13.97±0.10	13.04±0.02
	5.5740±0.0001	...	14.09±0.08	...
	5.57358±0.00001	13.52±0.01
	5.57372±0.00001	13.88±0.02
CFHQS J1509-1749	5.91572±0.00006	<13.4	14.11±0.14	13.04±0.06

